Heterogeneous tumor-immune microenvironments among differentially growing metastases in an ovarian cancer patient

Alejandro Jiménez-Sánchez[1], MSc, Danish Memon[1,2], PhD, Stephane Pourpe[11], MA, Harini Veeraraghavan[3], PhD, Yanyun Li[4], MD, PhD, Hebert Alberto Vargas[5], MD, Michael B Gill[1], PhD, Kay J. Park[6], MD, Oliver Zivanovic[7], MD, Jason Konner[8], MD, Jacob Ricca[4], BA, Dmitriy Zamarin[9], MD, PhD, Tyler Walther[11], BA, Carol Aghajanian[8], MD, Jedd D Wolchok[10], MD, PhD, Evis Sala[5], MD, PhD, Taha Merghoub[9], PhD, Alexandra Snyder[11,12,*], MD, Martin L Miller[1,*], PhD.

[1] Cancer Research UK Cambridge Institute, University of Cambridge, Li Ka Shing Centre, Robinson Way, Cambridge CB2 0RE, UK.
[2] European Molecular Biology Laboratory (EMBL), European Bioinformatics Institute, Wellcome Genome Campus, Hinxton, Cambridge CB10 1SD, UK.
[3] Department of Medical Physics, Memorial Sloan Kettering Cancer Center, 1275 York Avenue, New York, NY 10065, USA.
[4] Ludwig Collaborative/Swim Across America Laboratory, Memorial Sloan Kettering Cancer Center, New York, NY 10065, USA.
[5] Department of Radiology, Memorial Sloan Kettering Cancer Center, 1275 York Avenue, New York, NY 10065, USA.
[6] Department of Pathology, Memorial Sloan Kettering Cancer Center, 1275 York Avenue, New York, NY 10065, USA.
[7] Gynecology Service, Department of Surgery, Memorial Sloan Kettering Cancer Center, 1275 York Avenue, New York, NY 10065, USA.
[8] Gynecologic Medical Oncology Service, Department of Medicine, Memorial Sloan Kettering Cancer Center, 1275 York Avenue, New York, NY 10065, USA; Weill Cornell Medical College, New York, NY, USA.
[9] Ludwig Collaborative/Swim Across America Laboratory, Memorial Sloan Kettering Cancer Center, New York, NY 10065, USA; Department of Medicine Memorial Sloan Kettering Cancer Center, 1275 York Avenue, New York, NY 10065, USA.
[10] Ludwig Collaborative/Swim Across America Laboratory and Parker Institute for Cancer Immunotherapy, Memorial Sloan Kettering Cancer Center, New York, NY 10065, USA; Department of Medicine, Memorial Sloan Kettering Cancer Center, New York, NY 10065, USA; Department of Medicine, Weill Cornell Medical College, New York, NY 10065, USA; Immunology and Microbial Pathogenesis Programs, Weill Cornell Graduate School of Medical Sciences, New York, NY 10065, USA.
[11] Department of Medicine, Memorial Sloan Kettering Cancer Center, New York, NY 10065, USA.
[12] Department of Medicine, Weill Cornell Medical College, New York, NY 10065, USA.

*Correspondence: snyderca@mskcc.org, martin.miller@cruk.cam.ac.uk

Lead contact: Alexandra Snyder, MD.

Summary

We present an exceptional case of a patient with high-grade serous ovarian cancer, treated with multiple chemotherapy regimens, who exhibited regression of some metastatic lesions with concomitant progression of other lesions during a treatment-free period. Using immunogenomic approaches, we found that progressing metastases were characterized by immune cell exclusion while regressing and stable metastases were infiltrated by CD8+ and CD4+ T cells, and exhibited oligoclonal expansion of specific T cell subsets. We also detected CD8+ T cell reactivity against predicted neoepitopes after isolation of cells from a blood sample taken almost 3 years after the tumors were resected. These findings suggest that multiple distinct tumor immune microenvironments co-exist within a single individual and may explain in part the heterogeneous fates of metastatic lesions often observed in the clinic post therapy.

Introduction

The majority of patients with ovarian cancer relapse despite appropriate surgery and chemotherapy (Bowtell et al., 2015a; Cannistra, 2004). Ovarian cancer is characterized by a preponderance of DNA copy number alterations and a modest somatic missense mutation burden (~61 per exome) (Patch et al., 2015; TCGA et al., 2011). Analysis of data from various cancer types studied by the Cancer Genome Atlas (TCGA) consortium, including ovarian cancer, has demonstrated that the number of somatic mutations and neoepitopes (peptides resulting from somatic non-silent mutations that are presented to the immune system) correlates with overall survival (Brown et al., 2014). Together with the observation that chemotherapy in some cases may trigger immune activation in ovarian cancer and other cancer types (Galluzzi et al.,

2015; Gavalas et al., 2010; Pfirschke et al., 2016), this highlights the importance of investigating the host immune response in ovarian cancer. However, the interplay between somatic mutations, prior therapy, and the host immune response in this disease remains largely unknown.

Several studies of smaller cohorts of patients with metastatic ovarian cancer have found that primary and metastatic lesions exhibit heterogeneity at the genomic level (Bashashati et al., 2013; Lee et al., 2015; De Mattos-Arruda et al., 2014). Supporting these findings, functional magnetic resonance imaging (MRI)-based analysis has revealed that ovarian tumors and metastatic peritoneal implants are already phenotypically heterogeneous at diagnosis (Sala et al., 2012). As tumor heterogeneity increases the likelihood of presence of subclones able to escape the immune system (Bhang et al., 2015; Su et al., 2012; Turke et al., 2010), immune control may be particularly challenging in ovarian cancer due to extensive heterogeneity and the low number of potential mutation-derived epitopes.

The clinical challenge of tumor heterogeneity has been demonstrated recently in the context of immunotherapy: patients with less heterogeneous tumors, and hence, with more clonal neoepitopes, were more likely to respond to checkpoint blockade immunotherapy than patients with heterogeneous tumors (McGranahan et al., 2016). Whether chemotherapy and the immune system could work cooperatively is also being explored. In some settings, chemotherapy promotes immune cells homeostasis and activation (Carson et al., 2004; Gavalas et al., 2010; Pfirschke et al., 2016), tumor antigen release (Zitvogel et al., 2008), and decreased numbers of myeloid-derived suppressor cells in the tumor microenvironment (Suzuki et al., 2005). Furthermore, effector T cells have recently been implicated to play a role in abrogating fibroblast-

mediated chemoresistance in a mouse model of ovarian cancer (Wang et al., 2015). Despite these findings, a unified model describing the effect of chemotherapy on the tumor heterogeneity and immune-tumor interactions has not yet been reached. A critical step toward understanding the effect of chemotherapy on advanced metastatic diseases and the immune response in humans is to analyze intra-patient matched primary and metastatic tumors (Brabletz et al., 2013). The ability to perform such analyses has been limited by the fact that multiple tumor sites from a single patient with advanced disease are rarely concurrently sampled, mainly due to the lack of clinical indication.

Here we present a case study of a high-grade serous ovarian cancer patient whose different metastases exhibited concomitant regression and progression after treatment with multiple types of chemotherapy. We investigated the genetic, molecular, and cellular components that potentially underlie this differential growth using whole exome sequencing, RNA expression data, immunohistochemistry, neoepitope prediction, *in situ* T cell receptor sequencing of tumor infiltrating immune cells, and T cell-neoepitope challenge assays using intracellular cytokine staining (ICS). In this heavily chemotherapy-treated patient, immune cell infiltration with clonal expansion of T cells, but not mutation or neoepitope number, correlated with tumor progression/regression status. Our immunogenomic analysis paints a portrait that immune infiltration and activation is different in each tumor (at two years post chemotherapy). Inter-site immune heterogeneity represents an important clinical challenge in the development of treatment modalities to overcome intra-patient tumor heterogeneity.

Results

The patient presented here was diagnosed with stage IV high-grade serous ovarian adenocarcinoma, which typically exhibits a 5-year survival of 17% (National Cancer Institute, SEER Data Base), and underwent an optimal surgical debulking followed by paclitaxel combined with first cisplatin and then carboplatin. The patient experienced recurrence after 7 months, and during a period of 3 years, she was treated with multiple regimens of chemotherapy with progression of disease after each therapy (**Fig. 1A-B**). Her cancer was growing radiographically and her CA125 was rising during treatment with topotecan when she then transitioned to best supportive care and was followed clinically with regular CA125 biomarker evaluation. After chemotherapy treatment was stopped, she experienced an atypical course: her CA125 decreased, and after 2 years of clinical follow up, CT scans showed evidence of differential growth of metastatic lesions including a new complex cystic mass in the vaginal cuff. Because of her long treatment-free interval and abdominal discomfort, she opted to undergo another debulking procedure, which found a substantial disease burden including tumor implants on the liver capsule, the splenic hilum, right upper quadrant (RUQ) and recto-vaginal space (**Fig. 1A-B**). Samples of the primary and four metastatic tumors were submitted for whole exome sequencing, microarray RNA quantification, staining for protein markers by immunofluorescence, and *in situ* T cell receptor sequencing.

Phylogenetic analysis of somatic mutations in tumors

We performed whole exome sequencing of normal blood and the resected samples to identify somatic mutations in the primary tumor and the metastases. Of all samples, we detected the highest mutation load in the liver and vaginal cuff metastases (**Fig. 1C**). To infer the evolutionary relationship between the tumor samples, we used a

binary presence/absence matrix of the non-silent mutations to perform a phylogenetic reconstruction based on the parsimony ratchet analysis method with branch lengths proportional to the number of non-silent mutations (Nixon, 1999; Schliep, 2011) (**Fig. 1D** and **Fig. S1A**). The liver and vaginal cuff tumors were genetically more heterogeneous and harbored more mutations.

To estimate the proportion of cancer cells identified with a given mutation (cellular prevalence), we applied PyClone (Roth et al., 2014) using CopywriteR (Kuilman et al., 2015) inferred DNA copy number changes (**Fig. S1B-C**), and ABSOLUTE (Carter et al., 2012) inferred tumor purity and absolute copy numbers. As expected, truncal and shared mutations were generally clonal with high cellular prevalence, whereas private mutations had medium to low cellular prevalence indicating subclonal status (**Fig. 1E**). Focusing on the specific genes that were mutated across all samples, we found potential oncogenic driver alterations among the truncal mutations including *WNK3*^{P1728R}, *PAX4*^{P287L}, and *TP53*^{N247I} (**Fig. 1D**). *TP53*^{N247I} was detected with a high cellular prevalence indicating loss of heterozygosity, which was supported by our DNA copy number analysis. Additionally, we identified other putative truncal events including deletion of *BRCA1*, *BRCA2*, *PTEN*, and amplification of *CCNE1* (**Fig. S1B**), which are commonly altered in serous ovarian cancer (Bowtell et al., 2015b; Patch et al., 2015). Among the private mutations we detected several potential driver mutations including *RUNX3*^{P246S} in the growing splenic lesion and *CSMD1*^{G1770R} in the primary tumor. Several private and shared branch mutations were found in different Rho GTPase activating genes (ARHGAP) which inactivate Rho and Rac signaling involved in the control of cellular motility (Bernards and Settleman, 2004; Li et al., 2014).

Transcriptomic analysis reveals immune-related pathways over-expressed in regressing tumors

To evaluate if genes involved in chemotherapy resistance were differentially altered between tumors and associated with regression and progression status, we analyzed somatic alterations and gene expression data (Affymetrix transcript array) across the samples. After analyzing chemotherapy-resistance genes identified in HGSOC (Patch et al., 2015), as well as gene sets for multidrug resistance (ABC transporters), apoptosis, and DNA damage response, we found no clear evidence of gene expression or somatic alteration patterns (mutations, DNA amplification and deep deletion) that differed between progressing (primary, vaginal cuff, and spleen) and regressing/stable tumors (RUQ and liver) (**Fig. S2A-C**). Interestingly, there was a trend that the ABC transporter *TAP1*, which is known for its function as a transporter of cytosolic peptides to the endoplasmic reticulum for HLA class I presentation (Bahram et al., 1991; Neefjes et al., 1993; Powis et al., 1991; Suh et al., 1994), was expressed at a higher level in the regressing tumors (**Fig. 2A**).

To further identify potential differences between samples we analyzed gene sets and pathways in an unbiased manner with single sample Gene Set Enrichment Analysis (ssGSEA) (Barbie et al., 2009; Subramanian et al., 2005). Using permutation-based false discovery rate, we estimated the significance of the enrichment score for each pathway and performed an outlier analysis relating gene set significance to the relative change in enrichment score between a given sample and the rest of the samples (**Fig. 2B, Table S3 and S4**). The most significant and differentially enriched pathway found was the immune system pathway with a higher enrichment in the spleen and RUQ metastases, and a lower enrichment in the primary and vaginal cuff tumors (**Table S4B**).

Further indicating immune activation, the systemic lupus erythematosus pathway was highly enriched in the RUQ and liver metastases (**Table S4C**), while TCR signaling pathways were preferentially enriched in the RUQ sample alone (**Table S4D**). Cancer and proliferation pathways, as well as Wnt signaling, were more enriched in the primary and vaginal cuff tumors (**Table S4E**). No outlier gene sets were identified for the negatively enriched pathways (**Fig. S2E, Table S3**).

To investigate the gene expression differences between the samples on an unbiased individual gene level, we calculated the coefficient of variation of the expression levels for each gene across samples (**Table S2A**). We found that among the most variably expressed genes, besides lipid metabolic process-related genes in the liver, the T cell chemo-attractant CXCL9 was predominantly expressed in the RUQ and liver metastases, as well as STAT1, which has been implicated in the regulation of CXCL9 expression (Liao et al., 1995; Satoh and Tabunoki, 2013) (**Fig. S2D**). No relevant mutations in immune-related molecules were identified except for truncal mutations in the MHC class I polypeptide-related sequence B (*MICB*) (**Table S1A**), which is a stress-induced ligand recognized by NKG2D receptors on CD8αβ and γδ T cells, as well as NK cells (Bauer et al., 1999; Groh et al., 1999).

Heterogeneous immune cell infiltration in growing and regressing lesions

To investigate the immune infiltration status of the tumors, we analyzed tumor purity and overall stromal and immune components using ESTIMATE (Yoshihara et al., 2013). The lowest tumor purities and highest immune infiltration scores were found in the RUQ, liver and spleen samples (**Fig. 3A**). Furthermore, we deconvolved the gene

expression data using CIBERSORT (Newman et al., 2015) as a first approach to dissect infiltration of specific immune cell subsets in the tumors. We found that the largest immune cell components corresponded to CD8+ and CD4+ T cells in RUQ, liver, and spleen tumors, although the overall CIBERSORT deconvolution p-value was only significant for RUQ and liver tumors (**Fig. 3B**). In contrast, the primary and vaginal cuff tumors had low immune cell ESTIMATE scores and insufficient levels of immune cell transcripts to confidently apply CIBERSORT (**Table S5A-B**), together suggesting a low or absent immune component present in these tumors.

Following this analysis, samples were immuno-fluorescently co-stained for T cell markers CD4, CD8 and the T regulatory cell marker FOXP3, double stained for PD-L1 and macrophage marker CD68, as well as double stained for PD-L1 and the T cell marker CD3 (**Fig. 3C and S3A**). Consistent with the transcriptomic deconvolution analyses, the primary tumor demonstrated no T cell infiltration and was negative for PD-L1 and CD68 (**Fig. 3C-D, S3A, and Table S5C**). The vaginal cuff lesion, which was growing at the time of surgical resection, did display a T cell population, however, these cells bordered but did not infiltrate the tumor. The splenic lesion, which was also progressing at the time of resection, albeit at a much more modest rate than the vaginal cuff lesion, demonstrated a CD8+ infiltrate. Finally, the RUQ and liver metastases, which were regressing and stable respectively at the time of surgical resection, displayed a strong CD4+ and CD8+ infiltrate. In summary, the transcript and IF analyses suggested each tumor site displayed a unique tumor-immune microenvironment ranging from immune cell inclusion to exclusion.

Regressing metastases show T cell oligoclonal expansion

It is known that genetic alterations in HLA-I molecules are associated with escape of cancer cells from CD8+ T cell recognition (Shukla et al., 2015). The patient's HLA alleles were determined experimentally by conventional PCR-based HLA typing and computationally on exome data by OptiType (Szolek et al., 2014) and POLYSOLVER (Shukla et al., 2015) independently, yielding the same results (**Table S6A**). We searched copy number alterations, as well as mutations by applying POLYSOLVER – a specific computational pipeline for HLA-I typing and mutation detection in the HLA-I genes – however no genetic alterations were detected. We then assessed gene expression and found that all HLA-I genes were expressed in the tumors (**Table S2**), however, compared to primary and vaginal cuff samples, an overall higher expression of HLA genes was observed in the RUQ and liver samples, with a lesser extent seen in the spleen sample (**Fig. 4A**).

We next estimated the neoepitope landscape of the samples by mapping missense mutations to their amino acid sequences, *in silico* generating the mutant peptide sequences, and predicting the mutant peptide-HLA binding affinities to the patient's HLAs. The predictions were performed using the NetMHC algorithm with HLA specific cut-offs for HLA-I (Lundegaard et al., 2008; Nielsen et al., 2003; Paul et al., 2013) and consensus scores for HLA-II (Kim et al., 2012; Kreiter et al., 2015). The tumors with the highest mutation and neoepitope loads for both HLA class I and HLA class II were the liver and vaginal cuff, which also had the highest number of missense mutations (**Fig. 4B**). We also investigated if there were shared neoepitopes or mutations present in the RUQ (regressing) and liver (stable) metastases alone, i.e. not present in the other tumors. No shared mutations between RUQ and liver alone were detected

(**Fig. S4A**); therefore, it did not appear that a shared neoepitope or mutation alone explained the behavior of the non-progressing tumor sites.

As an active CD8 T cell infiltration can be a selective pressure at the neoepitope level (DuPage et al., 2012; Matsushita et al., 2012; Teng et al., 2015; Tran et al., 2016; Verdegaal et al., 2016), we further interrogated the neoepitope landscape by analyzing potential evidence of neoepitope depletion using an approach adopted from a report analyzing TCGA data (Rooney et al., 2015). Relative to the other samples of the patient, the regressing RUQ tumor showed a consistent – yet non-significant – tendency of neoepitope depletion (p<0.1 by two-sided empirical p-value, **Fig. S4B-C**). This result is in line with a recent report showing neoepitope depletion in tumors with higher levels of immune signatures in colorectal cancer (Davoli et al., 2017). We then predicted the intrinsic immunogenicity of neoepitopes by analyzing the biochemical properties of peptides that are predicted to be associated with T cell-epitope recognition (Calis et al., 2013). We observed that there was a significant effect of neoepitope clonality on the probability of a neoepitope having immunogenic properties, with clonal neoepitopes being predicted as less immunogenic (p=0.02 by chi-square test, **Fig. S5A-D**). Using the predicted non-binders instead of binders in a control analysis, the opposite trend was observed as there was a small but significant effect of clonal mutations being predicted as more immunogenic (p=0.003 by chi-square test, **Fig. S5F**). Although preliminary, these analyses indicate a potential negative selection process at the neoepitope level.

To evaluate a T cell response in the tumors, we investigated whether a T cell clonal expansion could be detected in the tumor samples. To this end, we performed *in situ* TCR sequencing on each sample and on peripheral blood from the patient sampled 550 days after tumor resection (**Fig. 4C, S6A, and Table S8**). We detected a T cell

expansion in the RUQ metastasis with a dominant clone accounting for 13% of all productive T cell receptors sequenced. The expanded clone was also detected in the liver and spleen metastases, and strikingly also in the blood of the patient. Though, the clonal frequency in the RUQ metastasis was significantly higher than the other samples (q<0.001 by two-sided binomial tests with BH correction). In contrast, no T cell receptors were detected in the primary and vaginal cuff tumors, further supporting their lack of T cell infiltrate.

Peripheral blood CD8+ T cells react against predicted neoepitopes

Since expanded T cell clones detected in the tumors were still detected in the patient's blood sampled 1 year 6 months (550 days) after resection, we decided to test whether circulating T cells could react against any of the predicted neoepitopes. We sampled blood from the patient again, this time at 2 years 8 months (978 days) after resection, and isolated peripheral blood mononuclear cells (PBMCs) (**Fig. S6A**). We performed an intracellular cytokine staining (ICS) assay lasting 21 days, where PBMCs were cultured with each of the mutant peptides (n=43) predicted to have at least one HLA-I neoepitope, as a mutant peptide (17mer) can have more than one predicted binder (9mer) (**Fig. S6B**). Importantly, the likelihood of observing T cell reactivity by the ICS assays is low due to the low frequency of T cell precursors in the blood and the limited representation of the total TCR repertoire in each peptide challenge experiment ($5x10^5$ cells per well) (Rizvi et al., 2014). Despite the high false negative rate generally observed with the ICS assay, we found CD8+ T cells reactive against several mutant peptides showing cytokine activation levels (INFγ and TNFα) similar to the positive control consisting of a mixture of viral-derived epitopes (**Fig. 5A-B, Table S8A**). Of the top five reactive peptides detected, all had a higher mutant to wild type predicted HLA-I

binding affinity (inset, **Fig. 5B**). With limited material available, we focused on the top hits and repeated the ICS experiment and again found reactivity with peptide 12, which was derived from a clonal mutation in *FLG2* E1608K (**Fig. S7**), and peptide 6, which was derived from a private mutation in *LRRC8E* in the spleen.

Discussion

The natural history of ovarian cancer typically features remissions of decreasing length, leading to premature death (Bowtell et al., 2015). In this unusual case, the divergent fates of the tumors show an overall association with multiple molecular and cellular features at the tumor-immune interface (**Fig. S8**). For example, the shrinking RUQ tumor was heavily infiltrated with CD4 and CD8 T cells and had evidence of active CD8 T cell surveillance with expansion of specific TCR clonotypes. The stable liver tumor also exhibited immune infiltration, but at a lower level and with fewer expanding T cell clones. The spleen tumor was growing modestly at the time of resection, and presented with intermediate tumor-immune microenvironment features. Finally, the growing vaginal cuff and the primary tumor exhibited complete immune cell exclusion. The TCR clone most prevalent in the non-progressing tumors was also detected in the blood of the patient 18 months after the metastases were resected, and clonal neoepitopes induced a CD8+ T cell response from PBMCs obtained nearly 3 years after surgery. The two most extreme tumors, the RUQ and the vaginal cuff, had a consistently divergent pattern of molecular features associated with immune activation (HLA expression, INFγ, CXCL9, TAP1 etc.) and immune suppression (Wnt signaling). Importantly, the observed features that relate to progression/regression status are correlative and do not *per se* prove any *bona fide* mechanism nor negate the fact that chemotherapy could have influenced the divergent fates. In sum, we find evidence of

distinct tumor-immune microenvironments among differentially growing metastases within the same individual.

Particular findings of this study may have important clinical implications if they are corroborated in large cohorts. In this patient with advanced HGSOC we observed distinct tumor immune microenvironments in the five sampled tumors (primary and four recurrent tumors). The mutation and predicted neoepitope space alone did not explain the different regressing/progressing behavior of the metastatic samples. In contrast to recent studies of resistance to immunotherapy, no mutations were detected in the antigen presentation machinery (Giannakis et al., 2016; Rooney et al., 2015; Shukla et al., 2015), beta2-microglobulin (Challa-Malladi et al., 2011; Rooney et al., 2015; Zaretsky et al., 2016), the IFN-gamma pathway (Benci et al., 2016; Zaretsky et al., 2016), or HLA-I molecules (Rooney et al., 2015; Shukla et al., 2015; Tran et al., 2016) in the growing tumors. Instead of specific neoepitopes present in regressing samples, T cell reactivity against clonal neoepitopes was detected. Interestingly, all neoepitopes that elicited a CD8+ T cell response had higher mutant to wild-type HLA-I predicted binding affinity. The lack of tumor specific somatic alterations in the regressing and stable tumors alone puts forward the idea that non-somatic factors in the tumor microenvironment may have been playing a critical role in the immune response and overall fate of the tumors. For example, STAT1 and CXCL9 were highly expressed in the RUQ and liver metastases; CXCL9 is well known as a potent T cell chemokine (Liao et al., 1995; Rainczuk et al., 2012) and high expression of CXCL9 and CXCL10 correlate with enhanced T cell infiltration of tumors and better survival of ovarian cancer patients (Bronger et al., 2016). In contrast, the vaginal cuff growing metastasis had a higher enrichment score in the Wnt pathway, which has been implicated as a mechanism that impairs recruitment of dendritic cells and prevents T cell infiltration in autochthonous mouse melanoma models

via a CXCL9 and CXCL10 dependent mechanism (Spranger et al., 2015, 2017). Although a direct link between tumor fate and the observations found in this patient cannot be proven with the available samples, this case emphasizes the importance of an integrative approach to understand the molecular mechanisms governing the interaction between the tumor and its immune microenvironment (Miao and Van Allen, 2016).

As in any case study, the present study has notable limitations. It involves only one patient, and thus further studies are needed to determine whether the principles discovered here apply to other patients. Furthermore, the interplay between treatment, somatic mutations, the immune system, and heterogeneous fates of the tumors cannot be untangled in this clinical case. For example, it is feasible that the multiple chemotherapy interventions for this patient contributed to shaping the somatic mutations and the microenvironment of the tumors, but due to the availability of samples and descriptive nature of the study this could not be explored further. Despite such limitations, this case provides evidence for differential tumor immune responses existing in metastases of the same individual, related not only to genetic alterations but also to the tumor-immune microenvironment, which to our knowledge has not yet been demonstrated in patients with ovarian cancer. Also, most studies on the tumor-immune microenvironment have been conducted in primary tumors (Teng et al., 2015), with the exception of a study of matched primary and metastatic tumors, which concluded that the immune contexture globally recapitulates that of the primary (Remark et al., 2013). In contrast, the case of recurrent HGSOC presented here clearly shows the opposite: that tumor-immune microenvironments, between primary tumor and metastases, and between metastases, can be heterogeneous within a patient.

Previous genomic and immune profiling of multiple lesions in patients have also shed light on tumor heterogeneity and its implications on tumor evolution (Gerlinger et al., 2012), disease progression (Ascierto et al., 2017), and immune control (McGranahan et al., 2016; Şenbabaoğlu et al., 2016; Sridharan et al., 2016). For example, tumors that are genetically more heterogeneous have less immune infiltrates (Şenbabaoğlu et al., 2016) and less benefit from checkpoint blockade immunotherapies (McGranahan et al., 2016). It has been shown that T cell infiltration and gene expression of immune related genes correlates with response to checkpoint blockade immunotherapy in melanoma (Chen et al., 2016). Additionally, analyses of synchronous resected metastases with differential progression in patients with melanoma has shown that intra-patient metastases present not only genetic heterogeneity, but also immune infiltration heterogeneity of immune cell types and T cell clonality between samples (Reuben et al., 2017). A rapid autopsy study of a patient with metastatic melanoma treated with anti-PD-1 therapy showed that resistant metastases overexpressed genes related to extracellular matrix and neutrophil function (Ascierto et al., 2017). Interestingly, association between Wnt siganlling and lack of T cell infiltration was also observed in a patient with adenoid cystic carcinoma where serial biopsies from the same patient were analyzed, and different expression profiles between primary and metastatic deposits where also detected (Sridharan et al., 2016). Finally, a plethora of molecular mechanisms and types of cells influencing the tumor immune microenvironment have been described in different tumor types leading to important advances in immunotherapy (Johanna A. Joyce, 2015; Melero et al., 2014; Sharma et al., 2017). Unfortunately, the promise of immunotherapy has not been as successful in ovarian cancer as it has been in other tumor types (Homicsko et al., 2016) despite it has been recognized more than a decade ago that T cell infiltration is a key element for patient outcome in this disease (Zhang et al., 2003). We believe that the growing evidence of differential genomic, transcriptomic, and

immune profiles between and within patients will eventually provide new key elements to target in ovarian cancer and other tumor types. However, this task will require extensive and deep systematic analyses along with longitudinal data, as the differences between metastases and coexistence of tumor immune microenvironments within a patient are likely to be dynamic and sensitive to intrinsic (e.g. mutations and cell-cell communication) and extrinsic perturbations (e.g. prior treatment and microbiome (Sivan et al., 2015; Vetizou et al., 2015)).

In conclusion, this case study provides evidence of divergent tumor genetics, tumor microenvironments, and immune activation within a single patient with advanced ovarian cancer. If this phenomenon proves generalizable, then the inter-site heterogeneity described here bespeaks a profound clinical challenge for the use of cytotoxic-, targeted-, and immunotherapies. This observation, while made in an exceptional long-term survivor patient, may explain the frequent heterogeneous responses seen clinically but insufficiently documented by the limited radiographic measurements provided by the Response Evaluation Criteria in Solid Tumors (RECIST). Given the data presented in this study, it will be essential to understand not only how to therapeutically target genomic heterogeneity between and within metastases, but also how to successfully mobilize an anti-tumor immune response able to control all metastases in advanced cancers.

Author Contributions

Aghajanian, Wolchok, Sala: study design, editing manuscript
Gill: analysis, editing manuscript
Jiménez-Sánchez: bioinformatics, analysis, study design, data interpretation, manuscript
Konner: patient's medical oncologist, study design
Li: pathologic evaluation, microscopy
Memon: ssGSEA analysis

Merghoub: study design related to IF and ICS, study design
Miller: study design, data interpretation, manuscript
Park: pathologic evaluation
Pourpe: design and execution of ICS experiments
Ricca, Zamarin: PD-L1, CD3 and CD68 staining and interpretation, editing manuscript
Snyder: study design, data interpretation, manuscript
Vargas: radiology outlines and tumor measurements, analysis
Veerarhagavan: radiology, analysis, manuscript
Walther: RNA isolation and expression
Zivanovic: patient's surgeon, study design

Acknowledgements

We acknowledge Dr Duncan Odom and Dr Tobias Janowitz (CRUK CI) for their insightful comments on the manuscript. We also thank Ron Gejman (MSKCC) for the HLA typing prediction of TCGA ovarian samples, Leon Chlon (CRUK CI) for his help on the CIBERSORT analysis, and Dr David Ochoa for his advice in the ssGSEA analysis. A.S. was supported by grants from the Marsha Rivkin Organization, Society of Memorial Sloan Kettering, Translational and Integrative Medicine Research Fund (MSKCC), Kaleidoscope of Hope and MSKCC core grant (P30 CA008748). M.M. was supported by Cancer Research UK core grant (C14303/A17197). A.J.S. was supported by a doctoral fellowship from the Cancer Research UK Cambridge Institute and the Mexican National Council of Science and Technology (CONACyT). D.M. is a fellow of the joint EMBL-EBI & NIHR Cambridge Biomedical Research Centre Postdoctoral (EBPOD) program.

References

Ascierto, M.L., Makohon-Moore, A., Lipson, E.J., Taube, J.M., McMiller, T.L., Berger, A.E., Fan, J., Kaunitz, G., Cottrell, T., Kohutek, Z., et al. (2017). Transcriptional mechanisms of resistance to anti-PD-1 therapy. Clin. Cancer Res. *23*, clincanres.0270.2016.

Bahram, S., Arnold, D., Bresnahan, M., Strominger, J.L., and Spies, T. (1991). Two putative subunits of a peptide pump encoded in the human major histocompatibility complex class II region. Proc. Natl. Acad. Sci. USA *88*, 10094–10098.

Barbie, D.A., Tamayo, P., Boehm, J.S., Kim, S.Y., Moody, S.E., Dunn, I.F., Schinzel, A.C., Sandy, P., Meylan, E., Scholl, C., et al. (2009). Systematic RNA interference reveals that

oncogenic KRAS-driven cancers require TBK1. Nature *462*, 108–112.
Bashashati, A., Ha, G., Tone, A., Ding, J., Prentice, L.M., Roth, A., Rosner, J., Shumansky, K., Kalloger, S., Senz, J., et al. (2013). Distinct evolutionary trajectories of primary high-grade serous ovarian cancers revealed through spatial mutational profiling. J. Pathol. *231*, 21–34.
Bauer, S., Groh, V., Wu, J., Steinle, a, Phillips, J.H., Lanier, L.L., and Spies, T. (1999). Activation of NK cells and T cells by NKG2D, a receptor for stress-inducible MICA. Science *285*, 727–729.
Benci, J.L., Xu, B., Qiu, Y., Wu, T.J., Dada, H., Twyman-Saint Victor, C., Cucolo, L., Lee, D.S.M., Pauken, K.E., Huang, A.C., et al. (2016). Tumor Interferon Signaling Regulates a Multigenic Resistance Program to Immune Checkpoint Blockade. Cell *167*, 1540–1554.e12.
Bernards, A., and Settleman, J. (2004). GAP control: Regulating the regulators of small GTPases. Trends Cell Biol. *14*, 377–385.
Bhang, H.C., Ruddy, D.A., Krishnamurthy Radhakrishna, V., Caushi, J.X., Zhao, R., Hims, M.M., Singh, A.P., Kao, I., Rakiec, D., Shaw, P., et al. (2015). Studying clonal dynamics in response to cancer therapy using high-complexity barcoding. Nat. Med. *21*, 440–448.
Bowtell, D.D., Böhm, S., Ahmed, A.A., Aspuria, P.-J., Bast, R.C., Beral, V., Berek, J.S., Birrer, M.J., Blagden, S., Bookman, M.A., et al. (2015a). Rethinking ovarian cancer II: reducing mortality from high-grade serous ovarian cancer. Nat. Rev. Cancer *15*, 668–679.
Bowtell, D.D., Böhm, S., Ahmed, A.A., Aspuria, P.-J., Bast, R.C., Beral, V., Berek, J.S., Birrer, M.J., Blagden, S., Bookman, M.A., et al. (2015b). Rethinking ovarian cancer II: reducing mortality from high-grade serous ovarian cancer. Nat. Rev. Cancer *15*, 668–679.
Brabletz, T., Lyden, D., Steeg, P.S., and Werb, Z. (2013). Roadblocks to translational advances on metastasis research. Nat Med *19*, 1104–1109.
Bronger, H., Singer, J., Windmüller, C., Reuning, U., Zech, D., Delbridge, C., Dorn, J., Kiechle, M., Schmalfeldt, B., Schmitt, M., et al. (2016). CXCL9 and CXCL10 predict survival and are regulated by cyclooxygenase inhibition in advanced serous ovarian cancer. Br. J. Cancer *115*, 553–563.
Brown, S.D., Warren, R.L., Gibb, E. a., Martin, S.D., Spinelli, J.J., Nelson, B.H., and Holt, R. a. (2014). Neo-antigens predicted by tumor genome meta-analysis correlate with increased patient survival. Genome Res. *24*, 743–750.
Calis, J.J.A., Maybeno, M., Greenbaum, J.A., Weiskopf, D., De Silva, A.D., Sette, A., Keşmir, C., and Peters, B. (2013). Properties of MHC class I presented peptides that enhance immunogenicity. PLoS Comput. Biol. *9*, e1003266.
Cannistra, S.A. (2004). Cancer of the Ovary. N Engl J Med *35124351*, 2519–2529.
Carson, W.E., Shapiro, C.L., Crespin, T.R., Thornton, L.M., and Andersen, B.L. (2004). Cellular immunity in breast cancer patients completing taxane treatment. Clin. Cancer Res. *10*, 3401–3409.
Carter, S.L., Cibulskis, K., Helman, E., McKenna, A., Shen, H., Zack, T., Laird, P.W., Onofrio, R.C., Winckler, W., Weir, B. a, et al. (2012). Absolute quantification of somatic DNA alterations in human cancer. Nat. Biotechnol. *30*, 413–421.
Challa-Malladi, M., Lieu, Y.K., Califano, O., Holmes, A.B., Bhagat, G., Murty, V. V., Dominguez-Sola, D., Pasqualucci, L., and Dalla-Favera, R. (2011). Combined Genetic Inactivation of β2-Microglobulin and CD58 Reveals Frequent Escape from Immune Recognition in Diffuse Large B Cell Lymphoma. Cancer Cell *20*, 728–740.
Chen, P.L., Roh, W., Reuben, A., Cooper, Z.A., Spencer, C.N., Prieto, P.A., Miller, J.P., Bassett, R.L., Gopalakrishnan, V., Wani, K., et al. (2016). Analysis of immune signatures in longitudinal tumor samples yields insight into biomarkers of response and mechanisms of resistance to immune checkpoint blockade. Cancer Discov. *6*, 827–837.
Cibulskis, K., Lawrence, M.S., Carter, S.L., Sivachenko, A., Jaffe, D., Sougnez, C., Gabriel, S., Meyerson, M., Lander, E.S., and Getz, G. (2013). Sensitive detection of somatic point mutations in impure and heterogeneous cancer samples. Nat. Biotechnol. *31*, 213–219.
Davoli, T., Uno, H., Wooten, E.C., and Elledge, S.J. (2017). Tumor aneuploidy correlates with markers of immune evasion and with reduced response to immunotherapy. Science (80-.). *355*, eaaf8399.
DuPage, M., Mazumdar, C., Schmidt, L.M., Cheung, A.F., and Jacks, T. (2012). Expression of tumour-specific antigens underlies cancer immunoediting. Nature *482*, 405–409.
Fabregat, A., Sidiropoulos, K., Garapati, P., Gillespie, M., Hausmann, K., Haw, R., Jassal, B.,

Jupe, S., Korninger, F., McKay, S., et al. (2016). The reactome pathway knowledgebase. Nucleic Acids Res. *44*, D481–D487.
Fisher, S., Barry, A., Abreu, J., Minie, B., Nolan, J., Delorey, T.M., Young, G., Fennell, T.J., Allen, A., Ambrogio, L., et al. (2011). A scalable, fully automated process for construction of sequence-ready human exome targeted capture libraries. Genome Biol. *12*, R1.
Galluzzi, L., Buqué, A., Kepp, O., Zitvogel, L., and Kroemer, G. (2015). Immunological Effects of Conventional Chemotherapy and Targeted Anticancer Agents. Cancer Cell *28*, 690–714.
Gavalas, N.G., Karadimou, A., Dimopoulos, M.A., and Bamias, A. (2010). Immune response in ovarian cancer: How is the immune system involved in prognosis and therapy: Potential for treatment utilization. Clin. Dev. Immunol. *2010*.
Gerlinger, M., Rowan, A.J., Horswell, S., Larkin, J., Endesfelder, D., Gronroos, E., Martinez, P., Matthews, N., Stewart, A., Tarpey, P., et al. (2012). Intratumor heterogeneity and branched evolution revealed by multiregion sequencing. N. Engl. J. Med. *366*, 883–892.
Giannakis, M., Mu, X.J., Shukla, S.A., Qian, Z.R., Cohen, O., Nishihara, R., Bahl, S., Cao, Y., Amin-Mansour, A., Yamauchi, M., et al. (2016). Genomic Correlates of Immune-Cell Infiltrates in Colorectal Carcinoma. Cell Rep. *15*, 857–865.
Gnirke, A., Melnikov, A., Maguire, J., Rogov, P., LeProust, E.M., Brockman, W., Fennell, T., Giannoukos, G., Fisher, S., Russ, C., et al. (2009). Solution hybrid selection with ultra-long oligonucleotides for massively parallel targeted sequencing. Nat. Biotechnol. *27*, 182–189.
Groh, V., Rhinehart, R., Secrist, H., Bauer, S., Grabstein, K.H., and Spies, T. (1999). Broad tumor-associated expression and recognition by tumor-derived gamma delta T cells of MICA and MICB. Proc. Natl. Acad. Sci. U. S. A. *96*, 6879–6884.
Hänzelmann, S., Castelo, R., and Guinney, J. (2013). GSVA: gene set variation analysis for microarray and RNA-Seq data. BMC Bioinformatics *14*, 7.
Homicsko, K., Hospitalier, C., Vaudois, U., and De, É.P.F. (2016). Targeting Programmed Cell Death 1 in Ovarian Cancer. *33*.
Johanna A. Joyce, D.T.F. (2015). T cell exclusion, immune privilege, and the tumor microenvironment. Science (80-.). *348*, 74–80.
Kanehisa, M., and Goto, S. (2000). KEGG: Kyoto encyclopedia of genes and genomes. Nucleic Acids Res. *27*, 29–34.
Kanehisa, M., Sato, Y., Kawashima, M., Furumichi, M., and Tanabe, M. (2015). KEGG as a reference resource for gene and protein annotation. Nucleic Acids Res. *44*, D457–D462.
Kim, Y., Ponomarenko, J., Zhu, Z., Tamang, D., Wang, P., Greenbaum, J., Lundegaard, C., Sette, A., Lund, O., Bourne, P.E., et al. (2012). Immune epitope database analysis resource. Nucleic Acids Res. *40*, 525–530.
Kotturi, M.F., Peters, B., Buendia-Laysa, F., Sidney, J., Oseroff, C., Botten, J., Grey, H., Buchmeier, M.J., and Sette, A. (2007). The CD8+ T-cell response to lymphocytic choriomeningitis virus involves the L antigen: uncovering new tricks for an old virus. J. Virol. *81*, 4928–4940.
Kreiter, S., Vormehr, M., van de Roemer, N., Diken, M., Löwer, M., Diekmann, J., Boegel, S., Schrörs, B., Vascotto, F., Castle, J.C., et al. (2015). Mutant MHC class II epitopes drive therapeutic immune responses to cancer. Nature *520*, 692–696.
Kuilman, T., Velds, A., Kemper, K., Ranzani, M., Bombardelli, L., Hoogstraat, M., Nevedomskaya, E., Xu, G., de Ruiter, J., Lolkema, M.P., et al. (2015). CopywriteR: DNA copy number detection from off-target sequence data. Genome Biol. *16*, 49.
Lee, J.-Y., Yoon, J.-K., Kim, B., Kim, S., Kim, M.A., Lim, H., Bang, D., and Song, Y.-S. (2015). Tumor evolution and intratumor heterogeneity of an epithelial ovarian cancer investigated using next-generation sequencing. BMC Cancer *15*, 85.
Li, H., Peyrollier, K., Kilic, G., and Brakebusch, C. (2014). Rho GTPases and cancer. BioFactors *40*, 226–235.
Liao, F., Rabin, R.L., Yannelli, J.R., Koniaris, L.G., Vanguri, P., and Farber, J.M. (1995). Human Mig chemokine: biochemical and functional characterization. J. Exp. Med. *182*, 1301–1314.
Liberzon, A., Subramanian, A., Pinchback, R., Thorvaldsdóttir, H., Tamayo, P., and Mesirov, J.P. (2011). Molecular signatures database (MSigDB) 3.0. Bioinformatics *27*, 1739–1740.
Lundegaard, C., Lund, O., and Nielsen, M. (2008). Accurate approximation method for prediction of class I MHC affinities for peptides of length 8, 10 and 11 using prediction tools trained on 9mers. Bioinformatics *24*, 1397–1398.

Matsushita, H., Vesely, M.D., Koboldt, D.C., Rickert, C.G., Uppaluri, R., Magrini, V.J., Arthur, C.D., White, J.M., Chen, Y.-S., Shea, L.K., et al. (2012). Cancer exome analysis reveals a T-cell-dependent mechanism of cancer immunoediting. Nature *482*, 400–404.

De Mattos-Arruda, L., Bidard, F.C., Won, H.H., Cortes, J., Ng, C.K.Y., Peg, V., Nuciforo, P., Jungbluth, A.A., Weigelt, B., Berger, M.F., et al. (2014). Establishing the origin of metastatic deposits in the setting of multiple primary malignancies: The role of massively parallel sequencing. Mol. Oncol. *8*, 150–158.

McGranahan, N., Furness, A.J.S., Rosenthal, R., Ramskov, S., Lyngaa, R., Saini, S.K., Jamal-Hanjani, M., Wilson, G.A., Birkbak, N.J., Hiley, C.T., et al. (2016). Immune Checkpoint Blockade. Science (80-.). *351*, 1463–1469.

Melero, I., Rouzaut, A., Motz, G.T., and Coukos, G. (2014). T-cell and NK-cell infiltration into solid tumors: A key limiting factor for efficacious cancer immunotherapy. Cancer Discov. *4*, 522–526.

Miao, D., and Van Allen, E.M. (2016). Genomic determinants of cancer immunotherapy. Curr. Opin. Immunol. *41*, 32–38.

Moutaftsi, M., Peters, B., Pasquetto, V., Tscharke, D.C., Sidney, J., Bui, H.-H., Grey, H., and Sette, A. (2006). A consensus epitope prediction approach identifies the breadth of murine T(CD8+)-cell responses to vaccinia virus. Nat. Biotechnol. *24*, 817–819.

Murugaesu, N., Wilson, G.A., Birkbak, N.J., Watkins, T.B.K., McGranahan, N., Kumar, S., Abbassi-Ghadi, N., Salm, M., Mitter, R., Horswell, S., et al. (2015). Tracking the genomic evolution of esophageal adenocarcinoma through neoadjuvant chemotherapy. Cancer Discov. *5*, 821–832.

Neefjes, J.J., Momburg, F., and Hammerling, G.J. (1993). Selective and ATP dependent translocation of peptides by the MHC encoded transporter. Science (80-.). *261*, 769–771.

Newman, A.M., Liu, C.L., Green, M.R., Gentles, A.J., Feng, W., Xu, Y., Hoang, C.D., Diehn, M., and Alizadeh, A. a (2015). Robust enumeration of cell subsets from tissue expression profiles. Nat. Methods *12*, 1–10.

Nielsen, M., and Lund, O. (2009). NN-align. An artificial neural network-based alignment algorithm for MHC class II peptide binding prediction. BMC Bioinformatics *10*, 296.

Nielsen, M., Lundegaard, C., Worning, P., Lauemøller, S.L., Lamberth, K., Buus, S., Brunak, S., and Lund, O. (2003). Reliable prediction of T-cell epitopes using neural networks with novel sequence representations. Protein Sci. *12*, 1007–1017.

Nixon, K.C. (1999). The Parsimony Ratchet, a New Method for Rapid Parsimony Analysis. Cladistics *15*, 407–414.

Patch, A.-M., Christie, E.L., Etemadmoghadam, D., Garsed, D.W., George, J., Fereday, S., Nones, K., Cowin, P., Alsop, K., Bailey, P.J., et al. (2015). Whole–genome characterization of chemoresistant ovarian cancer. Nature *521*, 489–494.

Paul, S., Weiskopf, D., Angelo, M.A., Sidney, J., Peters, B., and Sette, A. (2013). HLA Class I Alleles Are Associated with Peptide-Binding Repertoires of Different Size, Affinity, and Immunogenicity. J. Immunol. *191*, 5831–5839.

Peters, B., and Sette, A. (2005). Generating quantitative models describing the sequence specificity of biological processes with the stabilized matrix method. BMC Bioinformatics *6*, 132.

Pfirschke, C., Engblom, C., Rickelt, S., Cortez-Retamozo, V., Garris, C., Pucci, F., Yamazaki, T., Poirier-Colame, V., Newton, A., Redouane, Y., et al. (2016). Immunogenic Chemotherapy Sensitizes Tumors to Checkpoint Blockade Therapy. Immunity *44*, 343–354.

Powis, S., Townsend, A., Deverson, E., Bastin, J., Butcher, G., and Howard, J. (1991). Restoration of antigen presentation to the mutant cell line RMA-S by an MHC-linked transporter. Nature *354*, 528–531.

Rainczuk, A., Rao, J., Gathercole, J., and Stephens, A.N. (2012). The emerging role of CXC chemokines in epithelial ovarian cancer. Reproduction *144*, 303–317.

Remark, R., Alifano, M., Cremer, I., Lupo, A., Dieu-Nosjean, M.C., Riquet, M., Crozet, L., Ouakrim, H., Goc, J., Cazes, A., et al. (2013). Characteristics and clinical impacts of the immune environments in colorectal and renal cell carcinoma lung metastases: Influence of tumor origin. Clin. Cancer Res. *19*, 4079–4091.

Reuben, A., Spencer, C.N., Prieto, P.A., Gopalakrishnan, V., Reddy, S.M., Miller, J.P., Mao, X., De Macedo, M.P., Chen, J., Song, X., et al. (2017). Genomic and immune heterogeneity are associated with differential responses to therapy in melanoma. Npj Genomic Med. *2*, 10.

Rizvi, N.A., Hellmann, M.D., Snyder, A., Kvistborg, P., Makarov, V., Havel, J.J., Lee, W., Yuan, J., Wong, P., Ho, T.S., et al. (2014). Mutational landscape determines sensitivity to PD-1 blockade in non-small cell lung cancer. Science (80-.). *348*, 1–10.
Robinson, J.T., Thorvaldsdóttir, H., Winckler, W., Guttman, M., Lander, E.S., Getz, G., and Mesirov, J.P. (2011). Integrative genomics viewer. Nat. Biotechnol. *29*, 24–26.
Rooney, M.S., Shukla, S.A., Wu, C.J., Getz, G., and Hacohen, N. (2015). Molecular and Genetic Properties of Tumors Associated with Local Immune Cytolytic Activity. Cell *160*, 48–61.
Roth, A., Khattra, J., Yap, D., Wan, A., Laks, E., Biele, J., Ha, G., Aparicio, S., Bouchard-Côté, A., and Shah, S.P. (2014). PyClone: statistical inference of clonal population structure in cancer. Nat. Methods *11*, 396–398.
Sala, E., Kataoka, M.Y., Priest, a. N., Gill, a. B., McLean, M. a., Joubert, I., Graves, M.J., Crawford, R. a. F., Jimenez-Linan, M., Earl, H.M., et al. (2012). Advanced Ovarian Cancer: Multiparametric MR Imaging Demonstrates Response- and Metastasis-specific Effects. Radiology *263*, 149–159.
Satoh, J.I., and Tabunoki, H. (2013). A comprehensive profile of ChIP-Seq-based STAT1 target genes suggests the complexity of STAT1-mediated gene regulatory mechanisms. Gene Regul. Syst. Bio. *2013*, 41–56.
Schliep, K.P. (2011). phangorn: Phylogenetic analysis in R. Bioinformatics *27*, 592–593.
Şenbabaoğlu, Y., Gejman, R.S., Winer, A.G., Liu, M., Van Allen, E.M., de Velasco, G., Miao, D., Ostrovnaya, I., Drill, E., Luna, A., et al. (2016). Tumor immune microenvironment characterization in clear cell renal cell carcinoma identifies prognostic and immunotherapeutically relevant messenger RNA signatures. Genome Biol. *17*, 231.
Sharma, P., Hu-Lieskovan, S., Wargo, J.A., and Ribas, A. (2017). Primary, Adaptive, and Acquired Resistance to Cancer Immunotherapy. Cell *168*, 707–723.
Shukla, S. a, Rooney, M.S., Rajasagi, M., Tiao, G., Dixon, P.M., Lawrence, M.S., Stevens, J., Lane, W.J., Dellagatta, J.L., Steelman, S., et al. (2015). Comprehensive analysis of cancer-associated somatic mutations in class I HLA genes. Nat. Biotechnol. *33*.
Sidney, J., Assarsson, E., Moore, C., Ngo, S., Pinilla, C., Sette, A., and Peters, B. (2008). Quantitative peptide binding motifs for 19 human and mouse MHC class I molecules derived using positional scanning combinatorial peptide libraries. Immunome Res. *4*, 2–15.
Sivan, A., Corrales, L., Hubert, N., Williams, J.B., Aquino-Michaels, K., Earley, Z.M., Benyamin, F.W., Man Lei, Y., Jabri, B., Alegre, M.-L., et al. (2015). Commensal Bifidobacterium promotes antitumor immunity and facilitates anti-PD-L1 efficacy. Science (80-.). *350*, 1084–1089.
Spranger, S., Bao, R., and Gajewski, T.F. (2015). Melanoma-intrinsic β-catenin signalling prevents anti-tumour immunity. Nature *523*, 231–235.
Spranger, S., Dai, D., Horton, B., and Gajewski, T.F. (2017). Tumor-Residing Batf3 Dendritic Cells Are Required for Effector T Cell Trafficking and Adoptive T Cell Therapy. Cancer Cell *31*, 711–723.e4.
Sridharan, V., Gjini, E., Liao, X., Chau, N.G., Haddad, R.I., Severgnini, M., Hammerman, P., El-Naggar, A., Freeman, G.J., Hodi, F.S., et al. (2016). Immune Profiling of Adenoid Cystic Carcinoma: PD-L2 Expression and Associations with Tumor-Infiltrating Lymphocytes. Cancer Immunol. Res. *4*, 679–687.
Sturniolo, T., Bono, E., Ding, J., Raddrizzani, L., Tuereci, O., Sahin, U., Braxenthaler, M., Gallazzi, F., Protti, M.P., Sinigaglia, F., et al. (1999). Generation of tissue-specific and promiscuous HLA ligand databases using DNA microarrays and virtual HLA class II matrices. Nat. Biotechnol. *17*, 555–561.
Su, K.Y., Chen, H.Y., Li, K.C., Kuo, M.L., Yang, J.C.H., Chan, W.K., Ho, B.C., Chang, G.C., Shih, J.Y., Yu, S.L., et al. (2012). Pretreatment Epidermal Growth Factor Receptor (EGFR) T790M mutation predicts shorter EGFR tyrosine kinase inhibitor response duration in patients with non-small-cell lung cancer. J. Clin. Oncol. *30*, 433–440.
Subramanian, A., Tamayo, P., Mootha, V.K., Mukherjee, S., Ebert, B.L., Gillette, M.A., Paulovich, A., Pomeroy, S.L., Golub, T.R., Lander, E.S., et al. (2005). Gene set enrichment analysis: a knowledge-based approach for interpreting genome-wide expression profiles. Proc. Natl. Acad. Sci. U. S. A. *102*, 15545–15550.
Suh, W.-K., Cohen-Doyle, M.F., Fruh, K., Wang, K., Peterson, P.A., and Williams, D.B. (1994). Interaction of MHC class I molecules with the transporter associated with antigen processing.

Science (80-.). *264*, 1322–1326.
Suzuki, E., Kapoor, V., Jassar, A.S., Kaiser, L.R., and Albelda, S.M. (2005). Gemcitabine selectively eliminates splenic Gr-1+/CD11b + myeloid suppressor cells in tumor-bearing animals and enhances antitumor immune activity. Clin. Cancer Res. *11*, 6713–6721.
Szolek, A., Schubert, B., Mohr, C., Sturm, M., Feldhahn, M., and Kohlbacher (2014). OptiType: precision HLA typing from next-generation sequencing data. Bioinformatics *30*, 3310–3316.
TCGA, Sites, D., Bell, D., Berchuck, A., Birrer, M., Chien, J., Cramer, D.W., Dao, F., Dhir, R., Disaia, P., et al. (2011). Integrated genomic analyses of ovarian carcinoma. Nature *474*, 609–615.
Teng, M.W.L., Galon, J., Fridman, W.H., and Smyth, M.J. (2015). From mice to humans: Developments in cancer immunoediting. J. Clin. Invest. *125*, 3338–3346.
Thorvaldsdóttir, H., Robinson, J.T., and Mesirov, J.P. (2013). Integrative Genomics Viewer (IGV): High-performance genomics data visualization and exploration. Brief. Bioinform. *14*, 178–192.
Tran, E., Robbins, P.F., Lu, Y.-C., Prickett, T.D., Gartner, J.J., Jia, L., Pasetto, A., Zheng, Z., Ray, S., Groh, E.M., et al. (2016). T-Cell Transfer Therapy Targeting Mutant KRAS in Cancer. N. Engl. J. Med. *375*, 2255–2262.
Turke, A.B., Zejnullahu, K., Wu, Y.L., Song, Y., Dias-Santagata, D., Lifshits, E., Toschi, L., Rogers, A., Mok, T., Sequist, L., et al. (2010). Preexistence and Clonal Selection of MET Amplification in EGFR Mutant NSCLC. Cancer Cell *17*, 77–88.
Verdegaal, E.M.E., de Miranda, N.F.C.C., Visser, M., Harryvan, T., van Buuren, M.M., Andersen, R.S., Hadrup, S.R., van der Minne, C.E., Schotte, R., Spits, H., et al. (2016). Neoantigen landscape dynamics during human melanoma–T cell interactions. Nature *536*, 91–95.
Vetizou, M., Pitt, J.M., Daillere, R., Lepage, P., Waldschmitt, N., Flament, C., Rusakiewicz, S., Routy, B., Roberti, M.P., Duong, C.P.M., et al. (2015). Anticancer immunotherapy by CTLA-4 blockade relies on the gut microbiota. Science (80-.). *350*, 1079–1084.
Vita, R., Overton, J.A., Greenbaum, J.A., Ponomarenko, J., Clark, J.D., Cantrell, J.R., Wheeler, D.K., Gabbard, J.L., Hix, D., Sette, A., et al. (2015). The immune epitope database (IEDB) 3.0. Nucleic Acids Res. *43*, D405–D412.
Wang, P., Sidney, J., Dow, C., Mothé, B., Sette, A., and Peters, B. (2008). A systematic assessment of MHC class II peptide binding predictions and evaluation of a consensus approach. PLoS Comput. Biol. *4*.
Wang, P., Sidney, J., Kim, Y., Sette, A., Lund, O., Nielsen, M., and Peters, B. (2010). Peptide binding predictions for HLA DR, DP and DQ molecules. BMC Bioinformatics *11*, 568.
Wang, W., Kryczek, I., Dost??l, L., Lin, H., Tan, L., Zhao, L., Lu, F., Wei, S., Maj, T., Peng, D., et al. (2015). Effector T Cells Abrogate Stroma-Mediated Chemoresistance in Ovarian Cancer. Cell 1092–1105.
Yoshihara, K., Shahmoradgoli, M., Martínez, E., Vegesna, R., Kim, H., Torres-Garcia, W., Treviño, V., Shen, H., Laird, P.W., Levine, D.A., et al. (2013). Inferring tumour purity and stromal and immune cell admixture from expression data. Nat. Commun. *4*.
Zaretsky, J.M., Garcia-Diaz, A., Shin, D.S., Escuin-Ordinas, H., Hugo, W., Hu-Lieskovan, S., Torrejon, D.Y., Abril-Rodriguez, G., Sandoval, S., Barthly, L., et al. (2016). Mutations Associated with Acquired Resistance to PD-1 Blockade in Melanoma. N. Engl. J. Med. *375*, 819–829.
Zhang, L., Conejo-Garcia, J.R., Katsaros, D., Gimotty, P.A., Massobrio, M., Regnani, G., Makrigiannakis, A., Gray, H., Schlienger, K., Liebman, M.N., et al. (2003). Intratumoral T Cells, Recurrence, and Survival in Epithelial Ovarian Cancer. N. Engl. J. Med. *348*, 203–213.
Zitvogel, L., Apetoh, L., Ghiringhelli, F., and Kroemer, G. (2008). Immunological aspects of cancer chemotherapy. Nat. Rev. Immunol. *8*, 59–73.

Main figure titles and legends

Figure 1. Metastatic tumors exhibit heterogeneous growth and somatic mutation patterns after multi-line chemotherapy. A) Representative CT scans showing concomitant

progression/regression of the different resected metastatic tumors. RUQ=right upper quadrant. "Spleen" refers to the tumor deposit adjacent to the spleen. **B)** CT-based volume of metastatic lesions represented with the solid vertical lines**,** and dynamics of quantified CA125 levels with the red line indicating the CA125 upper limit of normal (35 Units/mL). The x-axis at the bottom shows a timeline of therapeutic interventions and clinical follow up. **C)** Number of missense, silent, and nonsense mutations. **D)** The phylogenetic tree represents the relationship of the samples based on binary calls of non-silent point mutations (**Table S1A**). Length of the branches is proportional to the number of mutations. Potential driver mutations are indicated. **E)** Hierarchical cluster analysis (Euclidean distance metric and "average" linkage method) of the cellular prevalence of point mutations (n=299) estimated with PyClone (Roth et al., 2014) (**Table S1B)**.

Figure 2. Differential expression of immune related pathways in heterogeneously growing tumors. A) Expression levels and genetic alterations of genes associated with chemotherapy resistance in HGSOC (Patch et al., 2015) and multidrug resistance. Amplification and deep deletion were defined as at least ±2 median absolute deviations of copy number alterations for each sample (**Fig. S1C**). **B)** Single sample gene set enrichment analysis (Barbie et al., 2009; Subramanian et al., 2005) of up-regulated pathways using the KEGG (Kanehisa and Goto, 2000; Kanehisa et al., 2015) and REACTOME (Fabregat et al., 2016) databases (**Table S3**). Significantly enriched pathways ($q < 0.05$) pathways with at least ±1 $\log_2$ change relative to the median of the other samples are colored (**Table S4**). False discovery rate adjusted *p*-value (*q*-value) was calculated using the Benjamini-Hochberg method.

Figure 3. Immune infiltration status shows heterogeneous microenvironments across tumor samples. A) Tumor purity and immune component estimated by analyzing Affymetrix-based transcriptomics (**Table S5A**) (Yoshihara et al., 2013). **B)** Fractions of immune cell subsets in tumor samples inferred from gene expression data using CIBERSORT (Newman et al., 2015). Width of bars is proportional to the $-\log_{10}$ p-value of the deconvolution (**Table S5B**). CIBERSORT empirical *p*-value, * $p<0.05$. **C)** Representative images of hematoxylin and eosin staining of tumor

samples and immunofluorescence staining for DAPI, cytotoxic T cells (CD8+), helper T cells (CD4+FOXP3-), T cells (CD3+), T-regs (CD4+FOXP3+), macrophages (CD68+), and immune-checkpoint PD-L1. Complete slides are shown in Figure S3. **D)** Image-based cell quantification of whole slides (**Table S5C**).

Figure 4. Higher HLA expression and T cell oligoclonal expansion detected in regressing tumors. A) HLA-I and II gene differential expression across samples (**Table S2**). **B)** Number of predicted neoepitopes per sample (**Table S6B-D**). **C)** TCR sequencing of FFPE tumor samples and blood. The most prevalent TCR clonotypes (top 5 for each sample and blood) are shown (**Table S8**). The blood sample was collected from the patient 550 days after secondary debulking (**Fig. S6A**). Inset shows detection of the most frequent TCR rearrangement (CASSNDEYRGPTYEQYF) and its abundance comparison between samples (two-sided binomial tests with Benjamini-Hochberg multiple test correction, *** q<0.001).

Figure 5. Predicted neoepitopes with higher mutant than wild-type HLA-I binding affinity elicit a T cell response. A) Representative scatter plots of TNF_{α} and IFN_{γ} intracellular cytokine staining of CD8+ T cells after 21 days of culture with CEF peptides or DMSO as positive and negative controls, or the predicted mutant peptides (**Fig. S6B**). CEF=Cytomegalovirus, Epstein-Barr virus, Influenza virus. **B)** Percentage of CD8+ T cells with double positive intracellular staining (TNF_{α} and IFN_{γ}) after incubation with each of the 43 predicted HLA-I neoepitopes, and HLA-I predicted binding affinity wild-type to mutant ratio (**Table S9A**). Mutation in gene *FLG2* (P12) was found clonal after manual inspection in IGV (**Fig S7A**).

Supplemental figure titles and legends

Figure S1. Non-silent somatic mutations and copy number alterations. A) Binary matrix of present/absent non-silent point mutations (n=188) used for the phylogeny tree reconstruction in Figure 1D (**Table S1A**). **B)** Relative copy number alterations inferred from WES data of the

primary and metastatic samples using CopywriteR (Kuilman et al., 2015). **C)** Relative copy number profiles and tumor purity inferred after ABSOLUTE (Carter et al., 2012) analysis. Amplified and deep deleted DNA segments were defined as copy number alterations with at least ±2 median absolute deviations for each sample. MAD = median absolute deviation.

Figure S2. Gene set analysis of transcript abundance and somatic alteration patterns across samples. A-C) Gene expression levels and genetic alterations of the DNA damage, apoptosis pathways, and caspases. **D)** Expression levels of the 50 most variant genes according to their coefficient of variation (**Table S2A**). **E)** Differential enrichment scores and enrichment *q*-values of down-regulated pathways between tumor samples (**Table S3**). Significantly enriched pathways ($q < 0.05$) pathways with at least ±1 $\log_2$ change relative to the median of the other samples are colored (**Table S4**). False discovery rate adjusted *p*-value (*q*-value) was calculated using the Benjamini-Hochberg method.

Figure S3. Complete slide hematoxylin and eosin, and immunofluorescent staining. A) Hematoxylin and eosin staining of tumor samples. Immunofluorescence staining for cytotoxic T cells (CD8+), helper T cells (CD4+FOXP3-), and regulatory T cells (CD4+FOXP3+).

Figure S4. Neoepitope distributions and HLA-I neoepitope depletion analysis. A) Number of unique and overlapping expressed missense mutations, HLA-I and II neoepitopes between samples (**Table S6D**). **B)** Correlations between expressed missense mutations and predicted HLA-I neoepitopes using NetMHC applied to TCGA ovarian samples (n = 150) and the primary and metastatic tumors (**Table S7A-C**). KDE=kernel density estimate. **C)** Top: Estimated neoepitope deviation from expected in the five tumor samples compared to TCGA ovarian cancer samples (n=150). The expected number of neoepitopes was calculated by taking into account the expected number of missense mutations and the number of silent mutations according to Rooney et al, 2015 (see Methods). Bottom: Neoepitope depletion analysis of 150 random unique permutations of the patient's tumors (primary, spleen, RUQ, liver, and vaginal cuff) and their

mutations. Each sample was compared against its own 150 unique permutations to control for the number of mutations (**Table S7D-E**). Two-sided empirical *p*-values were calculated from each distribution.

765

Figure S5. Predicted immunogenicity of HLA class I neoepitopes. A) Predicted immunogenic properties of trunk (clonal) and private HLA-I neoepitopes. Positive immunogenicity scores have biochemical properties associated with higher immunogenicity that outweigh properties associated with lower immunogenicity, and vice versa for negative scores (Calis et al., 2013). **B-**
770 **C)** Comparison between clonal and sub-clonal (including shared between two or more samples but not all) predicted immunogenicity of predicted binders and non-binders (two-sided Mann-Whitney rank test). **D-F)** Probability of an HLA-I neoepitope having immunogenic properties considering its clonality and HLA-I binding affinity using the neoepitope data in A, B, and C respectively. Clonal neoepitopes have a lower probability of having immunogenic properties than
775 sub-clonal predicted binders (chi-square test, p=0.02). For non-binders (NetMHC score > HLA-I specific cutoff), clonal neoepitopes have a higher probability of having immunogenic properties (chi-square test, p=0.003), as well as peptides with higher HLA-I affinities (chi-square test, p=0.0001), although the absolute differences are minor. No significant interaction between clonality and predicted HLA-I binding affinity was detected for either binders or non-binders.
780 GLM=generalized linear model.

Figure S6. PBMCs samples timeline and T cell-neoepitope recognition assay. A) Blood samples obtained from the patient 550 and 978 days after resection were used for TCR sequencing and T cell – neoepitope recognition assays respectively. **B)** Experimental setup and
785 flow cytometry gating strategy for the T cell –neoepitope recognition assays (intracellular cytokine staining assay) with surface staining of CD3, CD4, CD8, CD45, and intracellular staining of IL-4, IFN_{γ}, TNF_{α}. PBMC=peripheral blood mononuclear cells.

Figure S7. IGV screenshots of mutation *FLG2*^{E1608K}. A) From the mutant peptides that elicited a T cell response in the two independent experiments, peptide 12 comes from the mutation *FLG2*^{E1608K}. This mutation was originally called in all tumors expect the RUQ regressing tumor (**Table S1**). However, after manual inspection on IGV, we found that the mutation was present in the RUQ tumor as well, but at a very low level.

Figure S8. Overall associations between tumor fates and tumor-immune microenvironmental features. **A)** Cellular and molecular associations with change in tumor growth. Change in tumor growth (y-axis) was calculated by dividing the tumor volume at CT scan 11 by the tumor volume at CT scan 10 (**Fig. 1B**). Fitted curves are 2nd order polynomial regression lines plotted for trend visualization rather than prediction purposes. *Capase 1* and *4* are considered inflammatory caspases involved in a type of apoptosis related to immune response called pyroptosis. The enrichment score x-axis and the *q*-values come from the ssGSEA analysis. HLA-I genes include *HLA-A*, *B*, *C*, *E*, and *F*. HLA-II genes include *HLA-DPA1*, *DMA*, *DRA*, *DQA1*, *DMB*, *DPB1*, *DQB2*, *DRB5*, *DRB1*, *DQB1*, and *DOA*.

STAR Methods

Lead contact: Alexandra Snyder, MD.

Human subjects research

Patient samples were collected and analyzed after informed consent to the institutional tissue collection protocol, and approval by the Internal Review Board (IRB) of Memorial Sloan Kettering Cancer Center.

Tumor volume calculation

The two axes CT scan measurements and the equation for the ellipsoid volume (V = 4/3 * pi * a * b * c) were used to estimate tumor volumes, where a and b are the two axes and c is their mean.

Whole exome sequencing

Whole exome sequencing was performed using the Illumina protocol at the Broad Institute of MIT and Harvard, Cambridge, MA, USA. Illumina sequencing of exomes was employed targeting approximately 37.7Mb of mainly exonic territory made up of all targets from Broad Institute's Agilent exome design (Agilent SureSelect All Exon V2), all coding regions of Gencode V11 genes, and all coding regions of RefSeq gene and KnownGene tracks from the UCSC genome browser (http://genome.ucsc.edu). Data was analyzed using the Broad Picard Pipeline which includes de-multiplexing and data aggregation.

The Illumina exome sequencing uses Illumina's in-solution DNA probe based hybrid selection method that uses similar principles as the Broad Institute-AgilentTechnologies developed in-solution RNA probe based hybrid selection method (Fisher et al., 2011; Gnirke et al., 2009) to generate Illumina exome sequencing libraries. Pooled libraries were normalized to 2nM and denatured using 0.2N NaOH prior to sequencing. Flow cell cluster amplification and sequencing were performed according to the manufacturer's protocols using either the HiSeq 2000 v3 or HiSeq 2500. Each run was a 76 bp paired-end with a dual eight-base index barcode read. The sequencing depths of the samples were: normal blood sample (90% at 20X), primary (82% at 50X), spleen (78% at 50X), RUQ (60% at 50X), liver (89% at 50X), and vaginal cuff (77% at 50X) tumors.

Mutation calling

Reads with mapping quality below 30 in the BAM files were filtered out before mutation calling. Somatic single nucleotide variants (SNVs) were called using MuTect

version 1.1.4 (Cibulskis et al., 2013). Identified missense mutations were manually reviewed using the Integrative Genomics Viewer version 2.3.61 (Robinson et al., 2011; Thorvaldsdóttir et al., 2013).

Phylogenetic tree inference

The phylogenetic tree was generated as described in Murugaesu et al., 2015. A binary presence/absence matrix of all non-silent mutations was used as input for the R package phangorn version 2.0.2 (Schliep, 2011). UPGMA hierarchical clustering followed by the parsimony ratchet analysis (Nixon, 1999) were implemented to build the unrooted tree, and the acctran function was used to determine branch lengths.

Relative copy number alterations

To extract copy number information based on the sequenced exomes of the samples, CopywriteR version 2.2.0 (Kuilman et al., 2015) was employed in R version 3.2.3. To perform the analysis, mappability information based on the hg19 human reference genome, 20 kb bin size, and default parameters were used.

Absolute copy number alterations and tumor purity

The absolute copy number profiles and the tumor content of the samples were inferred using the computational method ABSOLUTE version 1.0.6 (Carter et al., 2012) in R version 3.2.3. ABSOLUTE integrates segmented copy number data, pre-computed statistical models of recurrent cancer karyotypes, allelic fractions of somatic SNVs, and a probabilistic model framework to jointly estimate candidate tumor purity, ploidy values, absolute copy number data, and subclonal single nucleotide variants (Carter et al., 2012). Tumor purity and absolute copy numbers were obtained using ABSOLUTE default parameters, segmented copy number data derived from CopywriteR, and variant

allele frequencies estimated by MuTect (Cibulskis et al., 2013). Best model selection was based on the guidelines provided by GenePattern and the Broad Cancer Genome Analysis group (http://www.broadinstitute.org/cancer/software/genepattern/analyzing-absolute-data). Amplifications and deep deletions were defined as copy number alterations with at least ±2 median absolute deviations for each sample copy number distribution as shown in Figure S1C.

Mutation cellular prevalence

Variant allelic cellular prevalence was estimated using PyClone version 0.13.0 (Roth et al., 2014) in Python version 2.7.11. The PyClone pipeline analysis was performed jointly on all samples with their tumor purity and absolute copy number alterations estimated by ABSOLUTE. Total copy number prior probability estimate and the PyClone binomial model were used in the analysis. The mutation variant allele frequencies, closest integer copy number alterations, and tumor purity were used as input. Mutations not present or called in the sample were set to 0. Agglomerative hierarchical cluster analysis with Euclidean distance metric and average linkage clustering was performed on the cellular prevalence values and samples. The *SREBF2*^{S120*} nonsense mutation was not included in the PyClone pipeline because its copy number data was closest to 0.

Gene expression

RNA was extracted from FFPE samples using the RecoverAll Total Nucleic Acid Isolation from Thermo Fisher Scientific (Catalog Number: AM1975). RNA expression was assessed using the human Affymetrix Clariom D Pico assay. Arrays were analyzed using the SST-RMA algorithm in the Affymetrix Expression Console Software. Expression was determined by using the Affymetrix Transcriptome Analysis Console,

and for genes displaying inconsistent expression between probes, the SRY gene signal was used as a cutoff.

Single sample gene set enrichment analysis

Single-sample GSEA (Barbie et al., 2009), a modification of standard GSEA (Subramanian et al., 2005), was performed on RNA measurements for each sample using the GSVA package version 1.24.1 (Hänzelmann et al., 2013) in R version 3.3.2 with parameters: `method='ssgsea'`, and `tau=0.25`. Normalized enrichment scores were generated for gene sets belonging to KEGG (Kanehisa and Goto, 2000; Kanehisa et al., 2015) and Reactome (Fabregat et al., 2016). The gene sets were obtained from MSigDB database version 5.2 (Liberzon et al., 2011). In order to identify significantly up- and down-regulated gene sets, a *p*-value was calculated for each gene set based on comparison of the enrichment score with 10,000 permutations of randomly sampled gene sets of the same size. All genes listed in the expression array were used to derive the permutated gene sets. Finally, the *p*-values were corrected using Benjamini and Hochberg (BH) method.

Immune cell gene expression signatures

Tumor purity and total immune component in the tumor samples were analyzed using the ESTIMATE algorithm method version 1.0.13 (Yoshihara et al., 2013) on the gene expression data using the option: `platform=affymetrix` in R version 3.4.0. Then, selection of probes with the highest variance for each gene was performed to deconvolute cell type specific immune signatures. The deconvolution was achieved using CIBERSORT Jar version 1.05 (https://cibersort.stanford.edu/) with the standard

LM22 signature gene file, and 1000 permutations to calculate deconvolution *p*-values (Newman et al., 2015).

Immunofluorescent staining

The immunofluorescent staining and cell counting were performed at Molecular Cytology Core Facility of Memorial Sloan Kettering Cancer Center using Discovery XT processor (Ventana Medical Systems) by a cytologist blinded to the sample identifiers and conditions. The tissue sections were deparaffinized with EZPrep buffer (Ventana Medical Systems), antigen retrieval was performed with CC1 buffer (Ventana Medical Systems). Sections were blocked for 30 minutes with Background Buster solution (Innovex) followed by avidin/biotin blocking for 8 minutes. Pseudocolors were applied as follows: CD4 A594, FOXP3 A488, CD8 A647; CD68 and CD3 A594 and PD-L1 A488. Cells were detected using the DAPI image, which was processed and segmented using ImageJ/FIJI (NIH). Appropriate threshold values were set for all other markers, and the number of cells with positive signal above the threshold was counted for all single and double staining.

For multiplex staining, each marker was added consecutively in separate staining runs as follows. CD4/FoxP3/CD8**:** Sections were incubated with anti-CD4 (Ventana, cat#790-4423, 0.5 µg/ml) for 5 hours, followed by 60 minutes incubation with biotinylated goat anti-rabbit IgG (Vector Laboratories, cat # PK6101) at 1:200 dilution. The detection was performed with Streptavidin-HRP D (part of DABMap kit, Ventana Medical Systems), followed by incubation with Tyramide Alexa 488 (Invitrogen, cat# T20922) prepared according to manufacturer instruction with predetermined dilutions. Next, slides were incubated with anti-FoxP3 (Abcam, cat#ab20034, 5 µg/ml) for 4 hours, followed by 60 minutes incubation with biotinylated horse anti-mouse IgG (Vector Laboratories, cat#

MKB-22258) at 1:200 dilution. The detection was performed with Streptavidin-HRP D (part of DABMap kit, Ventana Medical Systems), followed by incubation with Tyramide Alexa Fluor 568 (Invitrogen, cat# T20914) prepared according to manufacturer instruction with predetermined dilutions. Finally, sections were incubated with anti-CD8 (Ventana, cat#790-4460, 0.07 µg/ml) for 5 hours, followed by 60 minutes incubation with biotinylated goat anti-rabbit IgG (Vector, cat # PK6101) at 1:200 dilution.

PDL1/CD68 or CD3: First, sections were incubated with anti-PDL1 (Cell Signaling, cat#13684, 5 µg/ml) for 5 hours, followed by 60 minutes incubation with biotinylated goat anti-rabbit IgG (Vector, cat # PK6101) at 1:200 dilution. The detection was performed with Streptavidin-HRP D (part of DABMap kit, Ventana Medical Systems), followed by incubation with Tyramide Alexa 488 (Invitrogen, cat# T20922) prepared according to manufacturer instruction with predetermined dilutions. Next, slides were incubated with anti-CD68 (DAKO, cat#M0814, 0.02 µg/ml) for 5 hours, followed by 60 minutes incubation with biotinylated horse anti-mouse IgG (Vector Labs, cat# MKB-22258) at 1:200 dilution, or with anti-CD3 (DAKO, cat#A0452, 1.2 µg/ml) for 4 hours, followed by 60 minutes incubation with biotinylated horse anti-rabbit IgG (Vector Labs, cat# PK6101) at 1:200 dilution. The detection was performed with Streptavidin-HRP D (part of DABMap kit, Ventana Medical Systems), followed by incubation with Tyramide Alexa Fluor 568 (Invitrogen, cat# T20914) prepared according to manufacturer instruction with predetermined dilutions. After staining slides were counterstained with DAPI (Sigma Aldrich, cat# D9542, 5 µg/ml) for 10 min and cover slipped with Mowiol.

HLA typing

HLA class I and class II 6-digit typing was performed at the New York Blood Center by sequence-based typing and specific sequence primers; as well as the HLA

genotyping algorithms OptiType version 1.0 (Szolek et al., 2014) and POLYSOLVER version 1.0 (Shukla et al., 2015) with default parameters for HLA class I 4-digit typing. POLYSOLVER HLA-I typing and mutation calling were performed using samtools version 0.1.19 and novocraft 3.02.05 for the alignment, and MuTect version 1.1.7 for the variant calling.

Neoepitope predictions

In silico mutant peptide generation

To predict neoepitopes, "wild-type" petide 17mers (for HLA-I) and 29mers (for HLA-II) with the affected amino acid in the middle for each missense mutation were retrieved from the GRCh37.74 human reference proteome (http://ftp.ensembl.org/pub/release-74/fasta/homo_sapiens/pep/). To generate "mutant" peptides, the affected amino acid was replaced *in silico* with the corresponding mutant amino acid.

HLA class I epitope binding predictions

Mutant peptides were used as input for the T Cell Epitope Prediction Tools included in the Immune Epitope Database and Analysis Resource (IEDB) 3.0 (http://www.iedb.org/) (Vita et al., 2015). The HLA class I epitope binding predictions were performed using the HLA-I IEDB algorithms Consensus (Kim et al., 2012) and the artificial neural network (NetMHC) version 3.4 (Lundegaard et al., 2008; Nielsen et al., 2003) independently yielding same conclusions. For Consensus method – which combines NetMHC, the stabilized matrix method (Peters and Sette, 2005), and the combinatorial peptide libraries method (Sidney et al., 2008) – 9mers with a relative percentile rank ≤ 1% for each HLA-I allele were considered binders to cover most of the potential immune responses as previously suggested (Kotturi et al., 2007; Moutaftsi et

al., 2006). For NetMHC, different cut-off values were evaluated independently and compared between each other. 9mers with absolute IC_{50} affinity values ≤ HLA-I specific cutoffs were considered binders (http://help.iedb.org/entries/23854373) (Paul et al., 2013). HLA-I specific cut-offs were not available for HLA-I C alleles, therefore an IC_{50} ≤ 500nM was used instead. All mutant predicted binders were considered for the analyses, i.e. for each missense mutation, up to six binders for HLA-I (A, B, C alleles) and up to four binders for HLA-II (DQ and DR alleles). Since NetMHC gives actual nM binding affinities, and HLA-I specific cutoffs have been estimated, we used NetMHC predictions throughout the manuscript.

HLA class II epitope binding predictions

HLA class II epitope binding predictions on 15mers were performed using the HLA-II IEDB algorithms Consensus (Wang et al., 2008, 2010), NetMHCII version 2.2 (Nielsen and Lund, 2009), and Sturniolo (Sturniolo et al., 1999) since these were the only available methods for the patient HLA-II alleles. The Consensus method used the relative percentile ranks of NetMHCII and Sturniolo, and 15mers with percentile ranks ≤ 1% were considered binders. 15mers with NetMHCII IC_{50} ≤ 500nM or Sturniolo percentile rank ≤ 1% were considered binders, which are more stringent cut-off values than the IEDB recommended 1000nM for NetMHCII and ≤ 10% percentile rank for Sturniolo. In the authors' knowledge, HLA-II specific NetMHCII cut-offs have not been reported.

Neoepitope depletion analysis

TCGA ovarian cancer null model

To analyze neoepitope depletion across the different samples, we followed the

method developed by Rooney and colleagues using only expressed mutations. Commonly mutated genes were not included as indicated (Rooney et al., 2015). The method compares the samples to a data driven null model. To generate the null model and estimate neoepitope depletion, the nucleotide sequences flanking each mutation (context of the mutation) are taken into account. To control for tumor type differences, we used TCGA ovarian cancer samples to generate the null model (TCGA et al., 2011). Context of the mutations for the TCGA ovarian cancer samples and the case study tumor samples were obtained from the assembly of the Genome Reference Consortium Human Reference 37. Only TCGA ovarian cancer samples with mutation context in all missense and silent mutations were included (n=150). We predicted HLA-I neoepitopes of TCGA ovarian cancer samples using the same approach as for the case study samples described above.

Permutation null model

To compare the levels of neoepitope depletion only between the patient's samples, we generated sample specific null models based on 150 random unique permutations (redundant permutations excluded) of the samples and their mutations (**Table S7D**). The number of permutations was selected based on the number of samples used in the TCGA ovarian cancer neoepitope depletion analysis (n=150). Permutated and real samples were analyzed together using the same approach as for the TCGA ovarian cancer neoepitope depletion analysis described above. A permutation-based null model for each sample was used to control for the number of mutations.

Immunogenicity predictions

Immunogenic properties of HLA class I epitopes were estimated *in silico* using the IEDB resource tool "MHC I Immunogenicity" (http://tools.iedb.org/immunogenicity/), which combines the chemical and physical properties of the amino acids, their position in the epitope, and the HLA-I subtype allele to estimate the immunogenicity of a given neoepitope-HLA complex (Calis et al., 2013). To compare clonal and sub-clonal predicted immunogenic properties, we used two approaches: a) Mann-Whitney rank tests to compare absolute scores and b) binomial generalized linear models (GLM). The binomial GLM approach was considered appropriate for this setting because immunogenicity can be considered a binomial process, immunogenic or non-immunogenic. In this scenario, however, the binomial process corresponds to whether an epitope has biochemical properties associated with immunogenicity (score ≥ 0) that outweigh properties associated with no immunogenicity (score < 0). Importantly, predicted immunogenicity scores < 0 can still elicit an immunogenic response, but overall they have less immunogenic properties than positive scores (Calis et al., 2013). To further explain variation in the intrinsic immunogenic predictions we included HLA-I binding affinity (nM) as an explanatory variable. We then calculated the probability of a peptide having a positive immunogenic score or not based on the samples' neoepitope data. No interaction between clonality and HLA-I binding affinity was found, thus the interaction was excluded from the model. The final binomial GLM formula used is:

```
# R 3.4.0
m <-glm(data=data,immunogenicity~clonality+hla_binding,family=binomial)
```

TCR sequencing

High-throughput sequencing of the T cell receptors present in the samples and blood of the patient was done using the immunoSEQ assay platform (Adaptive biotechnologies).

Analysis of the sequences was performed on the immunoSEQ ANALYZER 3.0 (Adaptive biotechnologies). T cell rearrangements that are differentially abundant between samples were detected using the Differential Abundance tool by two-sided binomial tests with Benjamini and Hochberg multiple test correction, *q*-value < 0.01 was considered statistically significant.

PBMC – neoepitope assay

The predicted peptides were synthesized (Genscript Corporation). PBMCs were cultured in complete RPMI (Core Media Preparation Facility MSKCC) with peptides at 1 µg/mL, peptide vehicle (DMSO, Sigma-Aldrich) and CEF peptide pool (2µg/mL, C.T.L) for 21 days with peptide restimulation at day 7 and day 14. IL-2 (Proleukin, Chiron) and IL-15 (Peprotech, cat#200-15) were added every 3 days at 10 IU/mL and 10 ng/mL respectively. Intracellular Cell Staining (ICS) was performed at day 14, and day 21 after 6 hour re-stimulation in the presence of monensin for 5 hours (GolgiStop, BD). Cells were then stained for 15 min with viability dye (LIVE/DEAD Fixable Aqua Dead Cell Stain Kit, ThermoFisher) at 4°C followed by 30 min incubation with CD45-APC-H7 (BD Pharmingen, clone 2D1), CD3-Pacific Blue (BD Pharmingen, clone UCHT1), CD4-PerCP-Cy5.5 (eBioscience, clone OKT4), CD8-PE (BD Biosciences, clone SK1). Cells were then fixed and permeabilized with BD Cytofix/Cytoperm (BD Biosciences) for 20 min at 4°C and washed with BD Perm/Wash (BD Biosciences). The ICS was performed in BD Perm/Wash with IFNγ-FITC (eBioscience, clone GZ-4) and TNFα-PE-Cy (eBioscience, clone MAb11) at 4°C for 30 min. Samples were acquired on a BD LSRII flow cytometer (BD Biosciences) and the analysis was performed on FlowJo software (FlowJo, LLC).

Code availability

Code for the aforementioned bioinformatics will be shared upon request.

Supplemental tables

Table S1. Mutation data. A) Non-silent mutations in binary format. **B)** Mutation cellular prevalence. **C)** Log_2 gene expression of mutations after SST-RMA and LOESS normalizations. **D)** Log_2 gene expression of mutations after SST-RMA normalization. **E)** Gene expression of mutations in binary format (see methods).

Table S2. Gene expression data. A) Log_2 gene expression after SST-RMA and LOESS normalizations. **B)** Gene expression in binary format (see methods). **C)** Log_2 gene expression after SST-RMA.

Table S3. Single sample gene set enrichment analysis data. A) Enrichment scores after z-score normalization. **B)** Enrichment score *q*-values. **C)** Raw enrichment scores.

Table S4. Significantly differentially enriched pathways. A) Enrichment scores and *q*-values of significantly differentially enriched pathways**. B)** REACTOME immune system pathway genes. **C)** KEGG systemic lupus erythematosus genes. **C)** REACTOME T cell signaling pathway genes. **D)** KEGG Wnt signaling pathway genes.

Table S5. Tumor immune microenvironment data. A) ESTIMATE data. **B)** CIBERSORT data. **C)** Immunofluorescence whole slide quantification data.

Table S6. HLA and neoepitope prediction data. A) HLA genotypes. **B)** HLA-I neoepitope binding affinity predictions. **C)** HLA-II neoepitope binding affinity predictions. **D)** Expressed predicted binders.

Table S7. Neoepitope depletion data. A) Samples and predicted HLA-I binding affinity of expressed mutations. **B)** TCGA ovarian cancer samples and predicted HLA-I binding affinity of expressed mutations. **C)** Neoepitope depletion ratio of TCGA ovarian cancer samples and case study samples. **D)** Randomly permutated samples and predicted HLA-I binding affinity expressed muattions (see methods). **E)** Neoepitope depletion ratios of randomly permutated samples and real case study samples (see methods).

Table S8. TCR sequencing data.

Table S9. T cell-neoepitope challenge data.

1125

MAIN FIGURES

Jiménez-Sánchez *et al*, **"Heterogeneous tumor-immune microenvironments among differentially growing metastases in an ovarian cancer patient"**

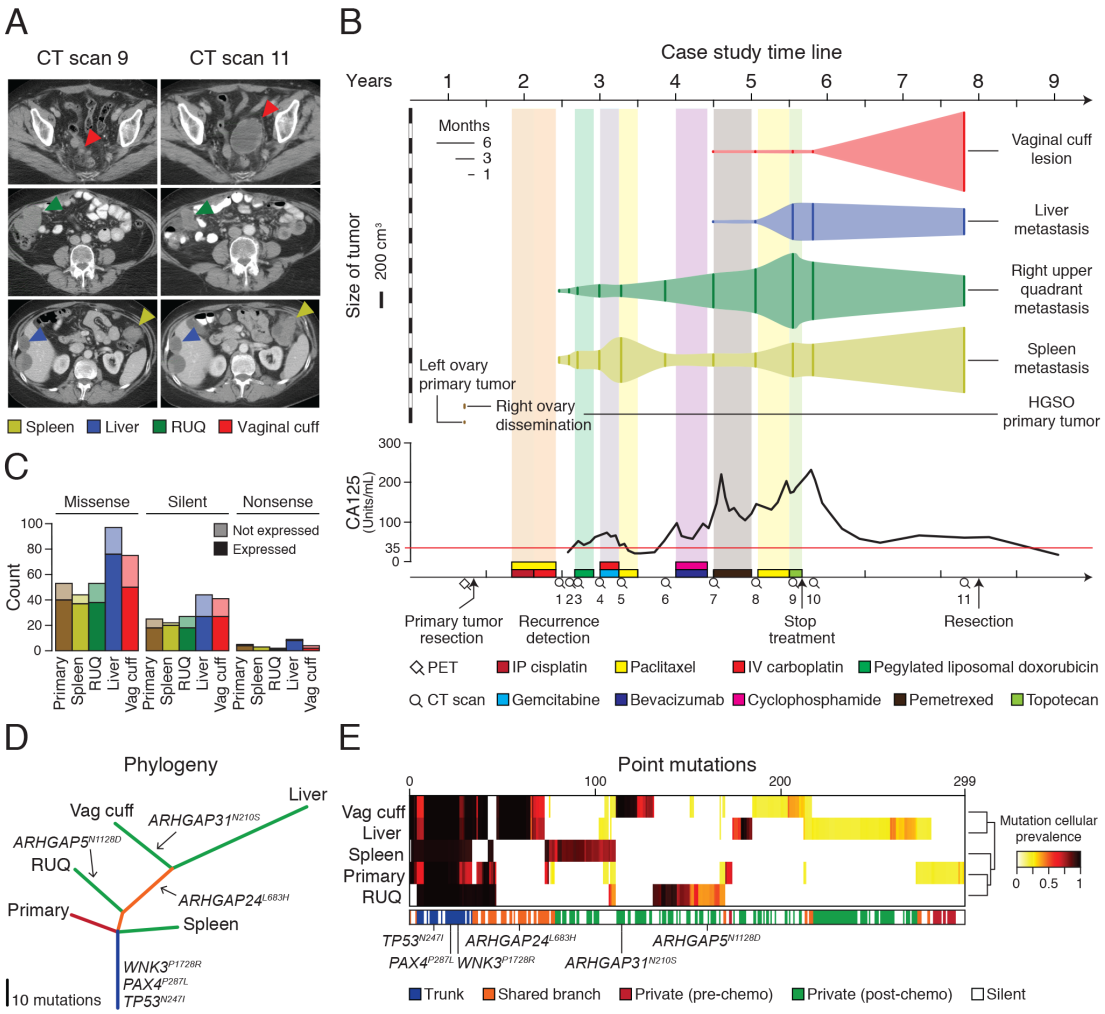

Figure 1. Metastatic tumors exhibit heterogeneous growth and somatic mutation patterns after multi-line chemotherapy. A) Representative CT scans showing concomitant progression/regression of the different resected metastatic tumors. RUQ=right upper quadrant. "Spleen" refers to the tumor deposit adjacent to the spleen. **B)** CT-based volume of metastatic lesions represented with the solid vertical lines**,** and dynamics of quantified CA125 levels with the red line indicating the CA125 upper limit of normal (35 Units/mL). The x-axis at the bottom shows a timeline of therapeutic interventions and clinical follow up. **C)** Number of missense, silent, and nonsense mutations. **D)** The phylogenetic tree represents the relationship of the samples based on binary calls of non-silent point mutations (**Table S1A**). Length of the branches is proportional to the number of mutations. Potential driver mutations

are indicated. **E)** Hierarchical cluster analysis (Euclidean distance metric and “average” linkage method) of the cellular prevalence of point mutations (n=299) estimated with PyClone (Roth et al., 2014) (**Table S1B)**.

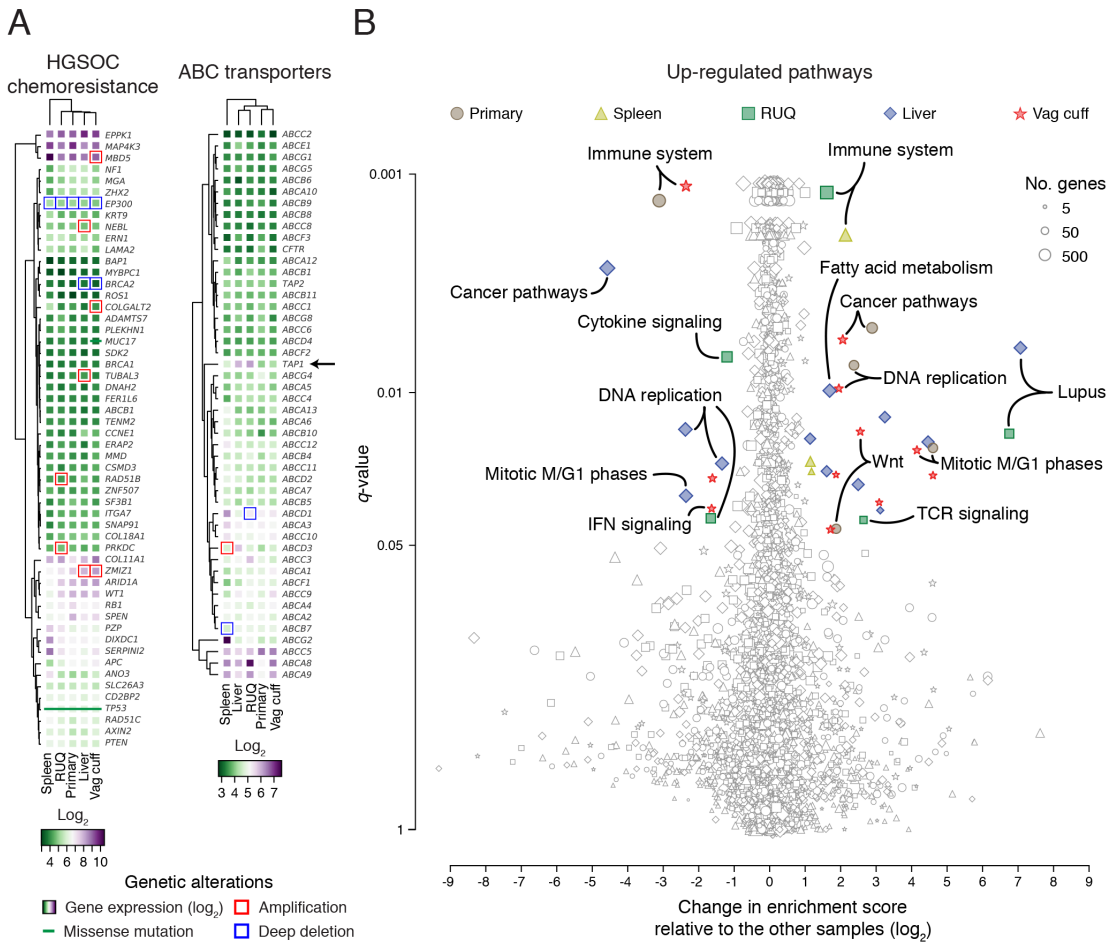

Figure 2. Differential expression of immune related pathways in heterogeneously growing tumors. A) Expression levels and genetic alterations of genes associated with chemotherapy resistance in HGSOC (Patch et al., 2015) and multidrug resistance. Amplification and deep deletion were defined as at least ±2 median absolute deviations of copy number alterations for each sample (**Fig. S1C**). **B)** Single sample gene set enrichment analysis (Barbie et al., 2009; Subramanian et al., 2005) of up-regulated pathways using the KEGG (Kanehisa and Goto, 2000; Kanehisa et al., 2015) and REACTOME (Fabregat et al., 2016) databases (**Table S3**). Significantly enriched pathways (q < 0.05) pathways with at least ±1 $\log_2$ change relative to the median of the other samples are colored (**Table S4**). False discovery rate adjusted p-value (q-value) was calculated using the Benjamini-Hochberg method.

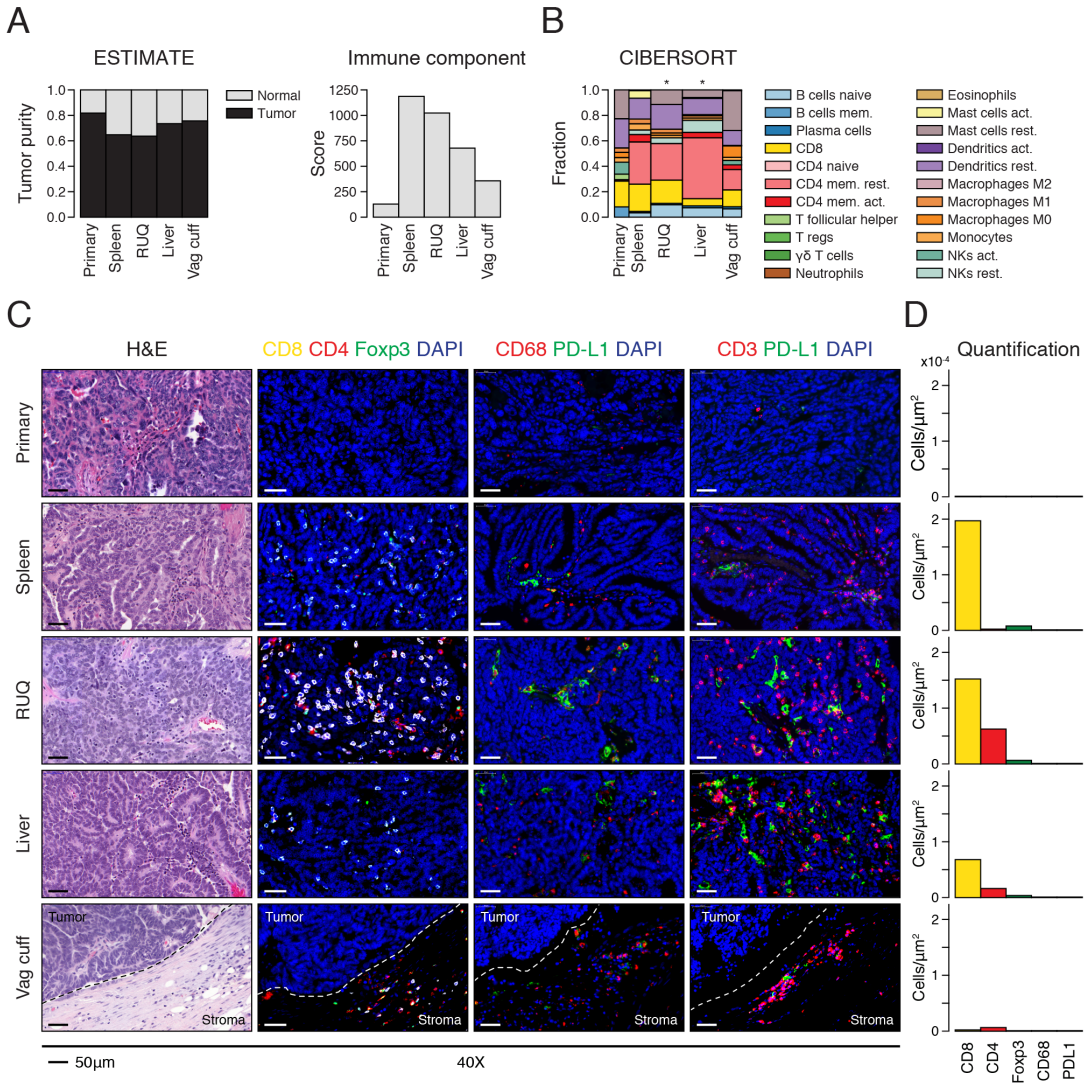

Figure 3. Immune infiltration status shows heterogeneous microenvironments across tumor samples. A) Tumor purity and immune component estimated by analyzing Affymetrix-based transcriptomics (**Table S5A**) (Yoshihara et al., 2013). **B)** Fractions of immune cell subsets in tumor samples inferred from gene expression data using CIBERSORT (Newman et al., 2015). Width of bars is proportional to the $-\log_{10}$ p-value of the deconvolution (**Table S5B**). CIBERSORT empirical *p*-value, * $p<0.05$. **C)** Representative images of hematoxylin and eosin staining of tumor samples and immunofluorescence staining for DAPI, cytotoxic T cells (CD8+), helper T cells (CD4+FOXP3-), T cells (CD3+), T-regs (CD4+FOXP3+), macrophages (CD68+), and immune-checkpoint PD-L1. Complete slides are shown in Figure S3. **D)** Image-based cell quantification of whole slides (**Table S5C**).

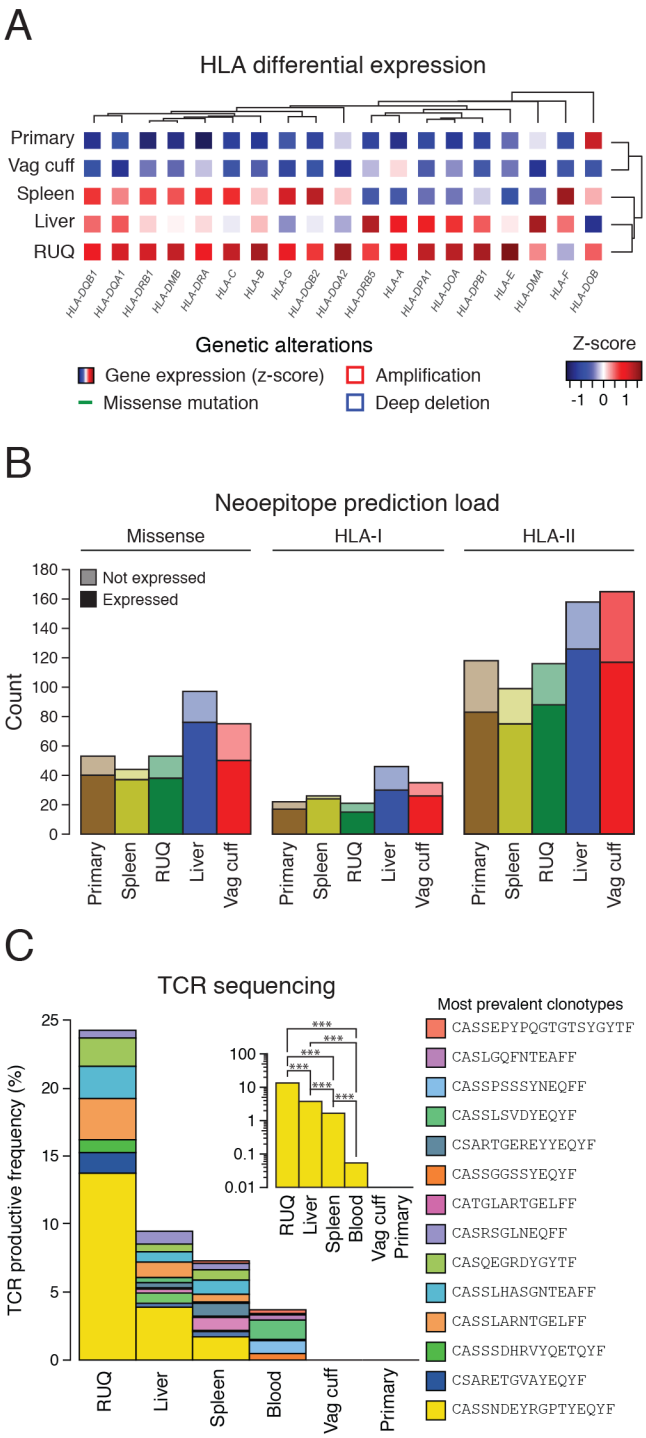

Figure 4. Higher HLA expression and T cell oligoclonal expansion detected in regressing tumors. **A)** HLA-I and II gene differential expression across samples (**Table S2**). **B)** Number of predicted neoepitopes per sample (**Table S6B-D**). **C)** TCR sequencing of FFPE tumor samples and blood. The most prevalent TCR clonotypes (top 5 for each sample and blood) are shown (**Table S8**). The blood sample was collected from the patient 550 days after secondary debulking (**Fig. S6A**). Inset shows detection of the most frequent TCR rearrangement (CASSNDEYRGPTYEQYF) and its abundance comparison between samples (two-sided binomial tests with Benjamini-Hochberg multiple test correction, *** q<0.001).

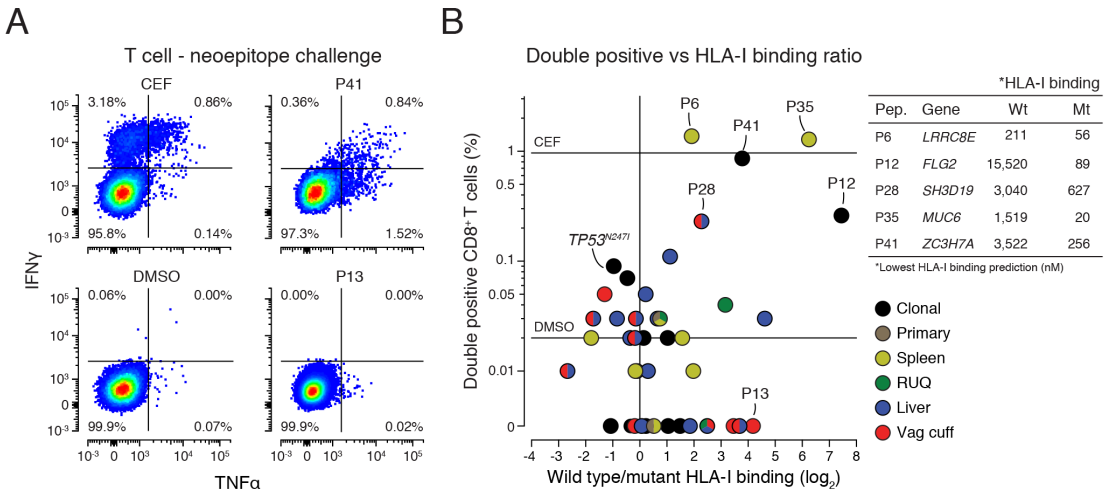

Figure 5. Predicted neoepitopes with higher mutant than wild-type HLA-I binding affinity elicit a T cell response. A) Representative scatter plots of TNF_{α} and IFN_{γ} intracellular cytokine staining of CD8+ T cells after 21 days of culture with CEF peptides or DMSO as positive and negative controls, or the predicted mutant peptides (**Fig. S6B**). CEF=Cytomegalovirus, Epstein-Barr virus, Influenza virus. **B)** Percentage of CD8+ T cells with double positive intracellular staining (TNF_{α} and IFN_{γ}) after incubation with each of the 43 predicted HLA-I neoepitopes, and HLA-I predicted binding affinity wild-type to mutant ratio (**Table S9A**). Mutation in gene *FLG2* (P12) was found clonal after manual inspection in IGV (**Fig S7A**).